Quaternary slip rates on the White Mountains fault zone, eastern California: Implications for comparing geologic to geodetic slip rates across the Walker Lane

Zachery M. Lifton[1,2,†], Jeffrey Lee[3,§], Kurt L. Frankel[1], Andrew V. Newman[1], and Jeffrey M. Schroeder[3]

[1]*School of Earth and Atmospheric Sciences, Georgia Institute of Technology, 311 Ferst Drive, Atlanta, Georgia 30332, USA*
[2]*Idaho Geological Survey, 322 East Front Street, Suite 201, Boise, Idaho 83702, USA*
[3]*Department of Geological Sciences, Central Washington University, 400 East University Drive, Ellensburg, Washington 98926, USA*

ABSTRACT

The White Mountains fault zone in eastern California is a major fault system that accommodates right-lateral shear across the southern Walker Lane. We combined field geomorphic mapping and interpretation of high-resolution airborne light detection and ranging (LiDAR) digital elevation models with ^{10}Be cosmogenic nuclide exposure ages to calculate new late Pleistocene and Holocene right-lateral slip rates on the White Mountains fault zone. Alluvial fans were found to have ages of $46.6 + 11.0/–10.0$ ka and $7.3 + 4.2/–4.5$ ka, with right-lateral displacements of 65 ± 13 m and 14 ± 5 m, respectively, yielding a minimum average slip rate of 1.4 ± 0.3 mm/yr. These new slip rates help to resolve the kinematics of fault slip across this part of the complex Pacific–North American plate boundary. Our results suggest that late Pleistocene slip rates on the White Mountains fault zone were significantly faster than previously reported. These results also help to reconcile a portion of the observed discrepancy between modern geodetic strain rates and known late Pleistocene slip rates in the southern Walker Lane. The total middle to late Pleistocene slip rate from the southern Walker Lane near 37.5°N was $7.9 + 1.3/–0.6$ mm/yr, ~75% of the observed modern geodetic rate.

INTRODUCTION

Understanding spatial and temporal variations in strain accumulation and release along plate boundaries is a fundamental problem in tectonics. Short-term and long-term slip rates are expected to be equal if the regional stress field remains unchanged over time, yet discrepancies between modern geodetic (10^1 yr) slip rates and long-term geologic (10^3–10^6 yr) slip rates are observed on several parts of the Pacific–North America plate boundary system (e.g., Bennett et al., 2003; Dolan et al., 2007; Frankel et al., 2007a, 2011; Oskin et al., 2008). Slip rate discrepancies have important implications for the evolution of faults and plate boundaries. For example, clarifying long- and short-term slip rates may lead to a better understanding of characteristic versus clustered earthquake rupture behavior (e.g., Gold and Cowgill, 2011; Wallace, 1987; Schwartz and Coppersmith, 1984). Also, discrepancies may imply that strain is distributed nonuniformly within a region of uniform far-field stress (e.g., Thatcher, 2009). However, it is not clear whether observed discrepancies are real or simply a manifestation of insufficient data. Calculating new slip rates (e.g., Frankel et al., 2011) and revisiting existing slip rates (e.g., Cowgill et al., 2009) have helped to reconcile some slip rate discrepancies; however, the slip rate discrepancy in the southern Walker Lane at ~37.5°N remains unresolved (e.g., Kirby et al., 2006; Frankel et al., 2007b; Lifton et al., 2013; Nagorsen-Rinke et al., 2013; DeLano et al., 2019).

The southern Walker Lane is a diffuse right-lateral shear zone, consisting of strike-slip faults and extensional step-over normal faults, that is interpreted to accommodate ~20% of the ~51 mm/yr of relative motion between the North American and Pacific plates (Figs. 1 and 2; Bennett et al., 2003; Wesnousky, 2005; Hammond and Thatcher, 2007; Lee et al., 2009b; DeMets et al., 2010). However, within parts of the southern Walker Lane, the contemporary geodetic deformation rate is ~1.4 times higher than the geologic deformation rate averaged over the late Pleistocene (Frankel et al., 2007b; Kirby et al., 2008; Lifton et al., 2013, 2015; Nagorsen-Rinke et al., 2013; DeLano et al., 2019). The two main right-lateral structures in the southern Walker Lane at 37.5°N latitude are the Fish Lake Valley fault and the White Mountains fault zone (Fig. 2). At this latitude, the Fish Lake Valley fault has accommodated up to $3.3 + 0.7/–0.1$ mm/yr of right-lateral motion since ca. 70 ka (Ganev et al., 2010; Frankel et al., 2011), while previously reported right-lateral slip rates on the White Mountains fault zone ranged from ~0.7–0.8 mm/yr since ca. 760 ka to ~0.3–0.4 mm/yr since ca. 22 ka (Kirby et al., 2006). To the east of Fish Lake Valley, faults in the Silver Peak–Lone Mountain extensional complex accommodate shear zone–parallel motion through extension, much like other step-over normal faults in the Walker Lane such as the Queen Valley fault (Lee et al., 2009b), Deep Springs fault (Lee et al., 2001b), and Tin Mountain fault (Fig. 2). Late Pleistocene extensional slip rates across the primary Silver Peak–Lone Mountain structures, the Emigrant Peak normal fault, Clayton Valley normal fault, and Lone Mountain normal fault, are $2.0 + 0.7/–0.5$ mm/yr (recalculated by Lifton et al. [2015] to estimate extensional slip rates from vertical slip rate data reported by Reheis and Sawyer, 1997), 0.1–0.3 mm/yr (Foy et al., 2012), and 0.7–0.8 mm/yr (Lifton et al., 2015), respectively. Additional middle to late Pleistocene slip is accommodated west of the White Mountains on distributed faults in the Volcanic Tableland (0.5 ± 0.2 mm/yr; DeLano et al., 2019) and the Round Valley fault (0.2 ± 0.1 mm/yr; Berry, 1997, recalculated by DeLano et al., 2019). In order to compare geologic slip rates to geodetic slip rates, we projected all horizontal geologic slip rates to the direction of relative motion between the Sierra Nevada–Great Valley and Central Great Basin blocks, 323° (Table 1; Bennett et al., 2003; Lifton et al., 2013). DeLano et al. (2019) built upon the sum of middle to

Zachery M. Lifton http://orcid.org/0000-0001-9508-9359

[†]zlifton@uidaho.edu.
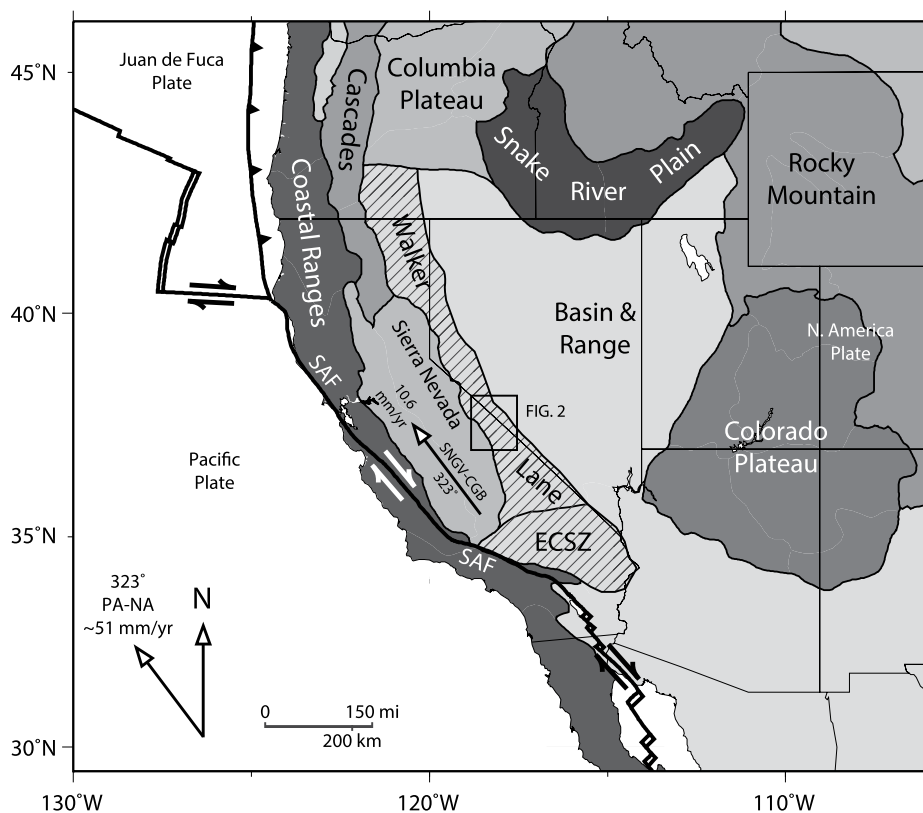[§]Also at: Department of Geophysics, Colorado School of Mines, Golden, Colorado 80401, USA.

Figure 1. Regional tectonic map of the western United States showing physiographic provinces (Fenneman and Johnson, 1946), plate boundaries, and relative plate motion between North American (NA) and Pacific (PA) plates (~51 mm/yr toward 323° at 37.5°N latitude). PA-NA relative velocity is from MORVEL model of DeMets et al. (2010). Also shown is the velocity vector of the relative motion between the Sierra Nevada–Great Valley (SNGV) and Central Great Basin (CGB) blocks (Bennett et al., 2003). ECSZ—Eastern California shear zone; SAF—San Andreas fault.

late Pleistocene geologic right-lateral slip rates across the southern Walker Lane at ~37.5°N presented by Lifton et al. (2013) by adding to that sum the minimum 323°-directed slip rates across the Round Valley fault (Berry, 1997), the Volcanic Tableland (DeLano et al., 2019), and the Lone Mountain fault (Lifton et al., 2015). Including these previously published data yielded a net minimum slip rate of 7.4 + 1.2/–0.6 mm/yr (Table 1). This summed middle to late Pleistocene right-lateral slip rate is ~70% of the geodetic rate of 10.6 ± 0.5 mm/yr (Lifton et al., 2013) modeled from global positioning system (GPS) data across the same area.

The source of the discrepancy between geologic and geodetic slip rates is not clearly known. While postseismic relaxation and other earthquake cycle effects may skew the observed geodetic slip rate, these effects are not likely to have a high enough magnitude to explain the ~1.4-fold discrepancy between geologic and geodetic slip rates. We suggest that at least part of the discrepancy is due to underestimation of

the previously calculated late Pleistocene slip rate on the White Mountains fault zone of 0.3–0.4 mm/yr (Kirby et al., 2006), especially since the White Mountains fault zone is the simplest kinematic connection for transfer of the relatively high slip rates on the Owens Valley fault (up to ~4.5 mm/yr; Lee et al., 2001a; Kirby et al., 2008; DeLano et al., 2019). We speculate that distributed deformation off of primary faults may also play a role in accommodating the discrepancy (e.g., Foy et al., 2012; Zinke et al., 2014; Gold et al., 2015; Milliner et al., 2015).

Late Pleistocene and Holocene slip rate estimates for the Owens Valley fault vary from ~0.6–1.6 mm/yr (Haddon et al., 2016) to 1.8 ± 0.3 mm/yr to 3.6 ± 0.2 mm/yr (Lee et al., 2001a), to 2.8–4.5 mm/yr (Kirby et al., 2008). Several research groups (e.g., Lee et al., 2001a; Sheehan, 2007; DeLano et al., 2019) have hypothesized that slip from the Owens Valley fault continues north onto the White Mountains fault zone. However, the previously estimated late Pleistocene slip rate on the White Mountains

fault zone is 0.3–0.4 mm/yr (Kirby et al., 2006), ~7%–67% of the right-lateral slip rate along the Owens Valley fault. This discrepancy in fault slip rates suggests that the previously estimated slip rate along White Mountains fault zone is too low, and/or transfer of right-lateral fault slip from the Owens Valley fault is, at least in part, partitioned northward into the Volcanic Tableland (Nagorsen-Rinke et al., 2013; DeLano et al., 2019). Reheis and Dixon (1996) and Lee et al. (2001a) hypothesized that the northward decrease in slip rate from the Owens Valley fault to the White Mountains fault zone may be attributed to slip transfer to the Fish Lake Valley fault via the Deep Springs normal fault. However, based on geodetic data, Lifton et al. (2013) suggested that most of the observed discrepancy between long- and short-term slip rates at the latitude of ~37.5°N may be occurring across Owens Valley. Thus, the White Mountains fault zone is an excellent candidate for reevaluating geologic slip rates.

In this study, we calculated two new right-lateral slip rates on the White Mountains fault zone using detailed field geomorphic mapping, interpretation of high-resolution light detection and ranging (LiDAR) digital elevation models, and ^{10}Be terrestrial cosmogenic nuclide (TCN) exposure ages applied to offset alluvial fans. We used these data to evaluate (1) the ~1.4-fold discrepancy in modern geodetic and late Pleistocene geologic slip rates, and (2) the discrepancy between the predicted slip transferred from the Owens Valley fault to the White Mountains fault zone.

Tectonic and Geologic Setting

The White Mountains constitute a north-northwest–trending block within the western boundary of the Basin and Range physiographic province (Fig. 2). The northern edge of the range is bound by the northeast-striking Queen Valley normal fault, and the southern edge of the range is adjacent to and continuous with the Inyo Range, but separated by the northeast-striking Deep Springs normal fault. The range is bound on the east side by the north-northwest–striking Fish Lake Valley right-lateral fault, and on the west by the right-lateral White Mountains fault zone. Rocks exposed within the range are Precambrian and Paleozoic metasedimentary rocks and Mesozoic metasedimentary and metavolcanic rocks intruded by numerous Mesozoic plutons related to the arc magmatism that created the Sierra Nevada batholith (Stockli et al., 2003; McKee et al., 1982; Hanson et al., 1987; Crowder et al., 1973; Krauskopf, 1971). The location and trend of the White Mountains fault zone appear to be controlled to some extent by
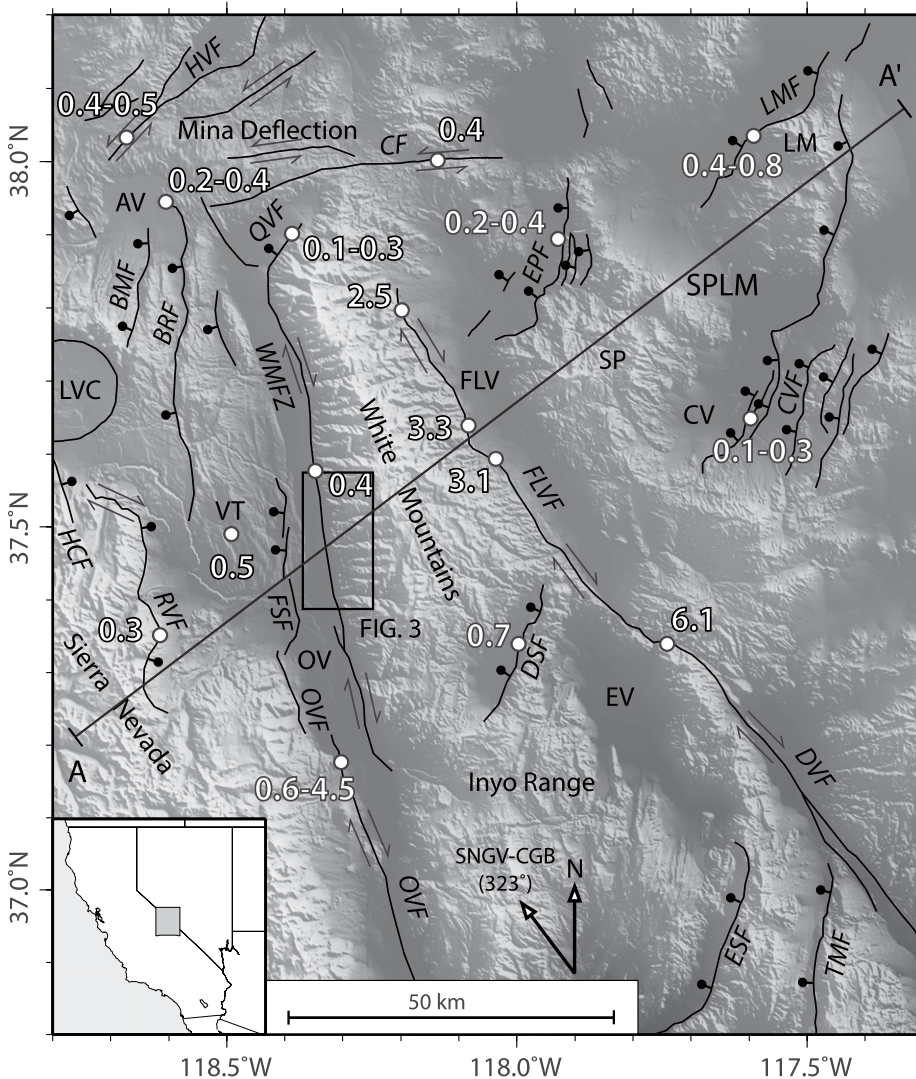
Figure 2. Shaded relief map of the southern Walker Lane showing major Quaternary faults. Black rectangle is extent of Figure 3. White filled circles are locations of geologic fault slip rates (white text; references below). Bar-and-ball pattern is located on the hanging wall of normal faults; arrow pairs indicate relative motion across strike-slip faults. Profile A–A′ is the approximate global positioning system (GPS) profile defined by Lifton et al. (2013) and shown as a velocity vector in Figure 12. Also shown is the velocity vector of the relative motion between the Sierra Nevada–Great Valley (SNGV) and Central Great Basin (CGB) blocks (Bennett et al., 2003). AV—Adobe Valley (Nagorsen-Rinke et al., 2013); BMF—Black Mountain fault; BRF—Benton Range fault (DeLano et al., 2019); CF—Coaldale fault; CV—Clayton Valley; CVF—Clayton Valley fault (Foy et al., 2012); DSF—Deep Springs fault (Lee et al., 2001b); DVF—Death Valley fault; EPF—Emigrant Peak fault (Reheis and Sawyer, 1997); ESF—Eureka-Saline fault; EV—Eureka Valley; FSF—Fish Slough fault; FLV—Fish Lake Valley; FLVF—Fish Lake Valley fault (Ganev et al., 2010; Frankel et al., 2011); HCF—Hilton Creek fault; HVF—Huntoon Valley fault; LM—Lone Mountain; LMF—Lone Mountain fault (Hoeft and Frankel, 2010; Lifton et al., 2015); LVC—Long Valley Caldera; OV—Owens Valley; OVF—Owens Valley fault (Lee et al., 2001a; Kirby et al., 2008; Haddon et al., 2016); QVF—Queen Valley fault (Lee et al., 2009b); RVF—Round Valley fault (Berry, 1997); SNGV-CGB—Sierra Nevada–Great Valley and Central Great Basin blocks; SP—Silver Peak Range; SPLM—Silver Peak–Lone Mountain; TMF—Tin Mountain fault; VT—Volcanic Tableland (DeLano et al., 2019); WMFZ—White Mountains fault zone (Kirby et al., 2006).

a preexisting Mesozoic shear zone along the western margin of the northern White Mountains (Stockli et al., 2003).

Structural and thermochronologic data from Stockli et al. (2003) suggest that the White Mountains fault zone initiated at ca. 12 Ma as a west-dipping normal fault with the inception of east-west extension, causing uplift and eastward tilting of the White Mountains block. At ca. 10–6 Ma, right-lateral strike-slip displacement began along the Fish Lake Valley fault on the east side of the White Mountains, accompanied by the formation of a shear-directed pull-apart basin in Fish Lake Valley (Stockli et al., 2003; Reheis and Sawyer, 1997). Normal faults of the White Mountains fault zone were reactivated as right-lateral strike-slip faults beginning ca. 3 Ma, accompanied by extension on Queen Valley and Deep Springs fault step-over transfer zones (Stockli et al., 2003; Lee et al., 2001a, 2001b, 2009b). Kirby et al. (2006) proposed that slip rates along the White Mountains fault zone decreased by a factor of 2–4 sometime between ca. 760 ka and ca. 70 ka, based on slip rates they calculated from offset volcanic tuff and debris-flow deposits. Historical seismic activity on the White Mountains fault zone includes the July 1986 M 6.2 Chalfant Valley earthquake, which produced small right-lateral oblique surface fractures (totaling 4.6–11.1 cm of displacement) along the White Mountains fault zone and within the Volcanic Tableland (Lienkaemper et al., 1987; dePolo and Ramelli, 1987; Smith and Priestley, 2000). The sequence of aftershocks trended to the northwest across Owens Valley, suggesting a possible kinematic link between the White Mountains fault zone and faults to the west.

Pliocene and Quaternary alluvial-fan deposits along the western side of the White Mountains are cut by a complex array of faults comprising the White Mountains fault zone (Figs. 3 and 4). Well-developed strike-slip geomorphic features, such as linear fault scarps, east- (up-fan-facing) and west-facing (down-fan-facing) fault scarps, offset alluvial fans, deflected drainages, closed depressions, ponded alluvium, and shutter ridges from Silver Canyon to Straight Canyon (Figs. 3 and 4), indicate active right-lateral slip along the White Mountains fault zone.

GEOLOGIC MAPPING

Based on our mapping along the length of the White Mountains fault zone, we identified a site (the "Estates site"), near the mouth of Piute Creek (Figs. 3 and 4), for a detailed study of Pleistocene and Holocene slip rates. The tectonic geomorphology here is likely well preserved because this location defines a compressional left step in a dextral fault system. Thus, erosional

TABLE 1. SUMMATION OF LONG-TERM GEOLOGIC SLIP RATES ACROSS THE SOUTHERN WALKER LANE, EASTERN CALIFORNIA

Fault	Reference	Reported rate (mm/yr)	Time scale (ka)	Direction of slip (degrees)	Recalculated slip rate[#] (mm/yr)	Slip rate toward 323° (mm/yr)
Lone Mountain fault (LMF)	Lifton et al. (2015)	0.7 ± 0.1	8	340	0.7 ± 0.1	0.7 ± 0.1
Clayton Valley fault (CVF)	Foy et al. (2012)	0.1–0.3	17	320	0.3 ± 0.1	0.3 ± 0.1
Emigrant Peak fault (EPF)	Reheis and Sawyer (1997)	3.4 + 1.8/–0.9*	6.5	315	2.0 + 1.0/–0.5	2.0 + 1.0/–0.5
Fish Lake Valley fault (FLVF)	Frankel et al. (2011)	3.3 + 0.7/–0.1	71	338	3.3 + 0.7/–0.1	3.2 + 0.7/–0.1
White Mountains fault zone (WMFZ)	Kirby et al. (2006)	0.7–0.8	760[§]	345	0.75 ± 0.05	0.7 ± 0.1
Volcanic Tablelands (VT)	DeLano et al. (2019)	0.5 ± 0.2	766	270	0.5 ± 0.2	0.3 ± 0.1
Round Valley fault (RVF)	Berry (1997)	0.3 ± 0.1[†]	15–25	270	0.3 ± 0.1	0.2 ± 0.1
Sum of previously published slip rates:						7.4 + 1.2/–0.6
Lone Mountain fault (LMF)	Lifton et al. (2015)	0.7 ± 0.1	8	340	0.7 ± 0.1	0.7 ± 0.1
Clayton Valley fault (CVF)	Foy et al. (2012)	0.1–0.3	17	320	0.3 ± 0.1	0.3 ± 0.1
Emigrant Peak fault (EPF)	Reheis and Sawyer (1997)	3.4 + 1.8/–0.9*	6.5	315	2.0 + 1.0/–0.5	2.0 + 1.0/–0.5
Fish Lake Valley fault (FLVF)	Frankel et al. (2011)	3.3 + 0.7/–0.1	71	338	3.3 + 0.7/–0.1	3.2 + 0.7/–0.1
White Mountains fault zone (WMFZ)	This study	1.4 ± 0.3	46.6	350	–	1.2 ± 0.3
Volcanic Tablelands (VT)	DeLano et al. (2019)	0.5 ± 0.2	766	270	0.5 ± 0.2	0.3 ± 0.1
Round Valley fault (RVF)	Berry (1997)	0.3 ± 0.1[†]	15–25	270	0.3 ± 0.1	0.2 ± 0.1
Sum including this study:						7.9 + 1.3/–0.6

*Vertical slip rate recalculated by Lifton et al. (2015) from original data reported in Reheis and Sawyer (1997), recalculated assuming 60° fault dip.

[†]Berry (1997) horizontal slip rate recalculated by DeLano et al. (2019).

[§]We used Kirby et al.'s (2006) larger middle Pleistocene slip rate here to be consistent with DeLano et al. (2019).

[#]In cases where published slip rates were reported as ranges or reported without uncertainties, we recalculated slip rates based on the original published data using the methods of Zechar and Frankel (2009).

incision along channels here occurs more rapidly compared to elsewhere because the compression causes local surface uplift, and shutter ridges and other records of tectonic activity are preserved (Lienkaemper et al., 1987). Mapping was done at 1:10,000 and 1:6000 scales on low-sun-angle aerial photographs and LiDAR hillshade digital elevation model (DEM) base maps, respectively (Fig. 5). Alluvial-fan units were differentiated and placed in a chronostratigraphic framework following the criteria of Bull (1991). These criteria include height above stream channels, degree of dissection, stratigraphy, soil profile development, degree of varnish, and pavement development. Alluvial-fan units are described in detail in Appendix A, and field photographs of the Q3a and Q4 surfaces can be found in Figures S1 and S2 of the supplemental online material.[1]

LiDAR data were collected along a swath covering a portion of the White Mountains fault zone (Lifton, 2012). Data were collected by the National Center for Airborne Laser Mapping (NCALM) on 4 July 2012 using an Optech Gemini Airborne Laser Terrain Mapper. The swath covered an area of ~40 km^2, with a point density of 9.6 points/m^2. Point cloud data were converted to a 1-m-resolution DEM by NCALM.

TCN EXPOSURE DATING

To determine exposure ages for the offset Q3a and Q4 alluvial-fan surfaces at the Estates site, we completed depth profiling of ^{10}Be, a terres-

trial cosmogenic nuclide (TCN). TCN exposure dating is based on the accumulation in the upper ~2 m of Earth's crust of cosmogenic nuclides, which are produced when cosmic rays interact with atomic nuclei in minerals (Lal, 1991; Gosse and Phillips, 2001). Exposure age is a function of several factors, including production rate (which varies with latitude and elevation), radioactive decay rate of the nuclide, and erosion of the surface. In depositional environments, such as alluvial fans, some TCNs may have accumulated in the sediment before it was deposited in the fan. This additional TCN concentration is referred to as inheritance and can be addressed through depth profiling (Anderson et al., 1996), in which TCN concentration is measured at increments below the surface. TCN production decreases quasi-exponentially with depth below the surface and is effectively zero at a depth of ~2–3 m, depending on material density. Thus, any TCN accumulation below the penetration depth of cosmic rays is inherited from previous exposure and can be treated appropriately when modeling ages.

TCN Sample Collection

We dug ~2-m-deep soil pits to sample TCNs in the Q3a and Q4 alluvial-fan surfaces (Fig. 5). Each pit was located on stable, near-horizontal surfaces away from risers and gullies along surface edges that are more affected by faster diffusive sediment transport processes. Five to seven ~1 kg samples of coarse sand and finer sediment were taken from 5- to 10-cm-thick surface-parallel horizons at different depths. Clast lithology included metasedimentary rocks, carbonates, and vein quartz. Samples within a given pit were collected from a single massive debris-flow deposit; we avoided sampling across unconformities. Schematic stratigraphic sections

of each depth profile pit can be found in Figure S3 of the supplemental online material.

In addition to subsurface samples, we also collected an amalgamated surface sample of quartz-rich clasts from each of the fan surfaces immediately surrounding the soil pits. The amalgamations consisted of 35 and 139 clasts for Q3a and Q4 surfaces, respectively. Surface clasts ranged in mass from 5 to 27 g, with approximate dimensions of 3 cm by 3 cm by 3 cm.

Samples were prepared at the Georgia Tech TCN Geochronology Laboratory following standard methods (e.g., Kohl and Nishiizumi, 1992), and the ^{10}Be/^{9}Be ratio of each sample was measured by accelerator mass spectrometry at the Center for Accelerator Mass Spectrometry at Lawrence Livermore National Laboratory (CAMS-LLNL). TCN analytical data can be found in Table 2. Sample preparation and analysis are described in detail in Appendix B.

TCN Exposure Age Modeling

We followed the methods of Hidy et al. (2010) to model our depth profiles and calculate exposure ages. The Hidy et al. (2010) model is a Monte Carlo simulator that takes into account site-specific geological constraints to find the most probable age, erosion rate, and inheritance, while propagating uncertainty for each. For our age models, we used a sea-level, high-latitude ^{10}Be production rate of 3.92 atoms g^{-1} yr^{-1}, scaled for the latitude and elevation of our sample locations (Lal, 1991; Stone, 2000; Nishiizumi et al., 2007; Borchers et al., 2016). Since the horizon was less than 12° in all directions, our samples did not require a topographic correction, and we used a shielding factor of 1. We allowed sediment density in the model to vary within a reasonable range for alluvial sediment, from 1.8 g/cm^3 to 2.4 g/cm^3. Erosion rate varied
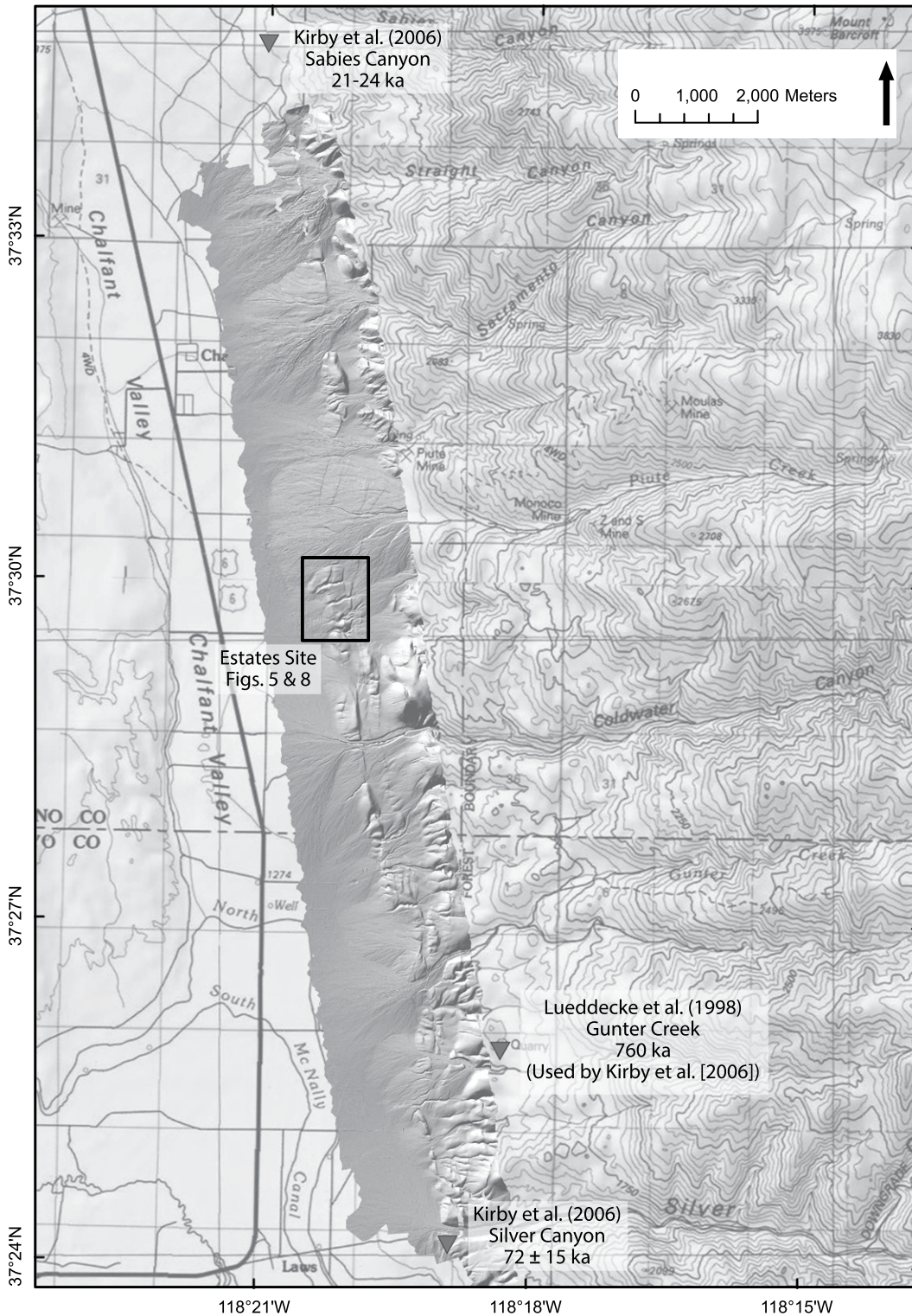
Figure 3. Hillshade map of airborne light detection and ranging (LiDAR) swath superimposed on portions of the U.S. Geological Survey (USGS) Laws and Chalfant Valley topographic quadrangle maps showing locations of the Estates site (black box) and locations of published ages for Pleistocene and Holocene Bishop Ash and alluvial fans. Hillshade illumination is from 315° azimuth and 45° elevation.

between −3 and 3 cm/k.y., while net erosion varied between −50 cm and 50 cm, with negative values representing aggradation. We allowed the inheritance values in the model to vary from a maximum equal to the concentration of the deepest sample to a minimum equal to half of that value. Screenshots of the model inputs are shown in Figure S10 of the supplementary online material.

We modeled fits to the depth profile concentrations and their respective 2σ uncertainties for the Q3a and Q4 fans. However, while the model was fit to the 2σ uncertainties of the concentrations, the resulting ages are reported with 1σ uncertainties to be consistent with other data in the study. The full model output is summarized in Tables S2 and S3 of the supplementary online material. It should be noted that the age results
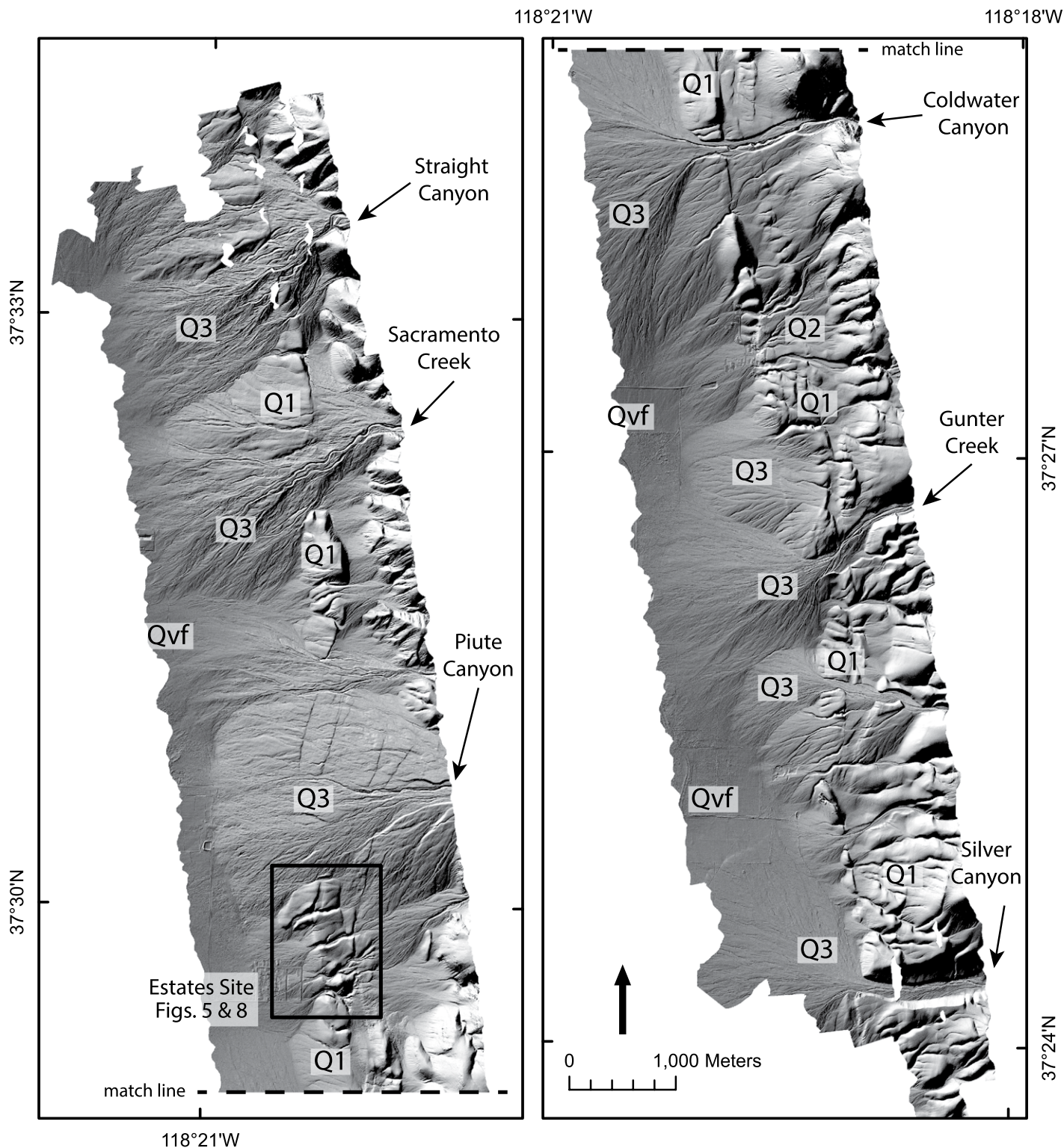
Figure 4. Detailed hillshade map of airborne light detection and ranging (LiDAR) swath showing the complexity of the White Mountains fault zone between Silver Canyon and Straight Canyon. The fault zone, characterized by both east- and west-facing fault scarps, cuts the older Q1 and Q2 alluvial-fan surfaces and has been eroded by the youngest of the Q3 alluvial-fan surfaces. Q3 surfaces interfinger with valley-fill deposits (Qvf). Location of hillshade map is shown in Figure 3. Hillshade illumination is from 315° azimuth and 45° elevation.

Figure 5. (A) Low-sun-angle aerial photograph (not orthorectified) of the Estates site. Scale is approximate. Aerial photograph was provided by Craig de Polo (1980s). (B) Hillshade map of the Estates site derived from 2012 airborne light detection and ranging (LiDAR) topographic data (Lifton, 2012). Hillshade illumination is from 315° azimuth and 45° elevation. (C) Geologic map superimposed on the LiDAR hillshade map of B showing the fault traces and displaced alluvial fans at the Estates site.

in Tables S2 and S3 are the direct output from the Hidy et al. (2010) depth profile model and vary slightly from the age results calculated by the Zechar and Frankel (2009) slip rate calculator. This difference is minor and is the result of rounding. The full age probability distribution function (PDF) from the Hidy et al. (2010) model was used as the input for the Zechar and Frankel (2009) slip rate calculator, so no data were changed or lost in the process of calculating slip rates. The Q3a depth profile consisted of four subsurface samples and one surface sample.

The modeled median exposure age and 1σ uncertainty for the Q3a fan are 46.6 + 11.0/–10.0 ka (Fig. 6). The Q4 depth profile consisted of six subsurface samples and one surface sample. We excluded from our model the sample at 38 cm depth because it is an outlier that did not follow the theoretical relationship between ^{10}Be concentration and depth. The modeled median exposure age and 1σ uncertainty for the Q4 fan are 7.3 + 4.2/–4.5 ka (Fig. 6). The modeled median inheritance and 1σ uncertainty are 10.4 + 0.25/–0.32 × 10^5 atoms/g for the Q3a depth profile and

7.6 + 0.21/–0.22 × 10^5 atoms/g for the Q4 depth profile (Fig. 6). These values suggest that the inherited component is a large proportion of the total TCN concentration, but the inheritance is well constrained by the depth profile approach.

Our fan exposure ages overlap, within uncertainty, with several published fan exposure ages in the Walker Lane, Eastern California shear zone, and Death Valley region (Fig. 7). Some of the previously published slip rates to which we compared our results were calculated from cosmogenic nuclide exposure ages derived with

TABLE 2. ANALYTICAL RESULTS FOR ^{10}Be COSMOGENIC NUCLIDE SURFACE EXPOSURE SAMPLES ALONG THE WHITE MOUNTAINS FAULT ZONE

Sample	Longitude (°W)	Latitude (°N)	Elevation (m)	Depth (cm)	Size fraction (μm)	Shielding factor*	Quartz (g)	Be carrier mass (g)	Be carrier concentration (ppm)	^{10}Be/^{9}Be†§ corrected for blank (×10^{-13})	^{10}Be concentration# (atoms/g)	^{10}Be concentration error (atoms/g)	AMS error§ (%)	Total measured error** (%)
Q4														
WM-11-03a	118.33387	37.49553	1388	183–193	125–710	1	33.8531	0.2929	1354	10.00 ± 0.19	780241	16571	2.12	3.28
WM-11-03b				145–155	125–710	1	38.0837	0.2926	1354	11.25 ± 0.21	779935	16520	2.12	3.28
WM-11-03c				105–115	125–710	1	56.6096	0.2985	1354	16.59 ± 0.51	790252	25409	3.22	4.07
WM-11-03d				75–85	125–710	1	45.1364	0.2969	1354	12.99 ± 0.24	771304	16330	2.12	3.28
WM-11-03e				55–65	125–710	1	44.5907	0.2928	1354	13.00 ± 0.24	770487	16296	2.11	3.27
WM-11-03f				38–44	125–710	1	71.4777	0.2925	1354	17.04 ± 0.55	629758	21316	3.38	4.21
WM-11-04				0		1	87.9044	0.3093	1354	27.02 ± 0.52	858583	18744	2.18	3.32
Q3a	118.33408	37.49924	1408											
WM-11-08b				120–130	250–710	1	46.5856	0.3058	1354	18.47 ± 0.42	1094780	27032	2.47	3.51
WM-11-08c				80–87	250–710	1	46.7700	0.3057	1354	19.83 ± 0.37	1170734	24599	2.10	3.27
WM-11-08d				50–60	250–710	1	46.5875	0.3065	1354	22.87 ± 0.43	1359230	29057	2.14	3.29
WM-11-08e				30–37	250–710	1	39.7717	0.3063	1354	19.03 ± 0.36	1323124	28351	2.14	3.29
WM-11-06				0		1	105.1283	0.3103	1354	55.76 ± 0.22	1487481	60446	4.06	4.77

*Horizon is <12° in all directions, and so no geometric correction was necessary.
†Isotopic ratios were normalized to standard 07KNSTD3110 with a value of 2.85 × 10^{-12} (Nishiizumi et al., 2007).
§Uncertainties reported at 1σ confidence level.
#Samples were corrected for background using blank values of 125,455 ± 15,852 for WM-11-04 and WM-11-06; 72,957 ± 9,365 for WM-11-03; and 89,208 ± 11,621 for WM-11-08.
**Total measured error includes a 2.5% 1σ error in sample preparation added in quadrature to the 1σ AMS error (e.g., Hidy et al., 2010; Gosse and Phillips, 2001).

an earlier, larger ^{10}Be production rate of 4.76 atoms g^{-1} yr^{-1} (Lal, 1991; Stone, 2000; Nishiizumi et al., 2007). A lower production rate yields relatively older ages than a higher production rate. Because the availability and reporting of the original data vary widely, we did not recalculate previously published ages and slip rates. Given similar climate across these regions at similar times, fan deposition would have occurred synchronously, and fan ages will tend to cluster into groups (Bull, 1991; Machette et al., 2008). The overlap of our fan ages with clusters of other fan ages in the region lends confidence to the accuracy of our exposure ages.

FAULT GEOMETRY, GEOMORPHOLOGY, AND SLIP MAGNITUDE

The White Mountains fault zone is ~500–1000 m wide and consists of up to four subparallel strands that cut through the alluvium along the western range front of the White Mountains (Figs. 4, 5, and 8). The average strike of the fault zone is ~353°; the average strike at the Estates site is ~348°. The White Mountains fault zone fault scarps are generally west facing, although in several places they face east. The alternation between west- and east-facing scarps along short sections of the fault scarp suggests that the apparent vertical offset is the result of lateral displacement of high topography juxtaposed against low topography, as well as a minor extensional component. Scarps along the entire White Mountains fault zone range in height from 1 to 4 m.

Fault displacement measurements were made from the 1-m-resolution LiDAR DEM using the Lateral Displacement Calculator (LaDiCaoz) MATLAB software package (Zielke and Arrowsmith, 2012). LaDiCaoz treats the cross-sectional profiles of stream channels or fan risers as waveforms. The user defines a fault plane, a cross-sectional profile of the offset stream channel on each side of the fault, and the angle at which the offset channel projects onto the fault. One channel profile is stretched, vertically shifted, and horizontally translated along the fault plane relative to the second profile in order to get the best fit between offset channels. We used channels, channel walls, and alluvial-fan risers as offset markers when backslipping the fault. LaDiCaoz calculates a fit quality parameter (with units of m^{-1}) when matching channel profiles, but it does not explicitly calculate uncertainties in displacement measurements. LaDiCaoz provides an "optimum" displacement but not upper and lower bounds to define uncertainties. To estimate uncertainties of displacement measurements, we tested three to five different backslipped reconstructions around each
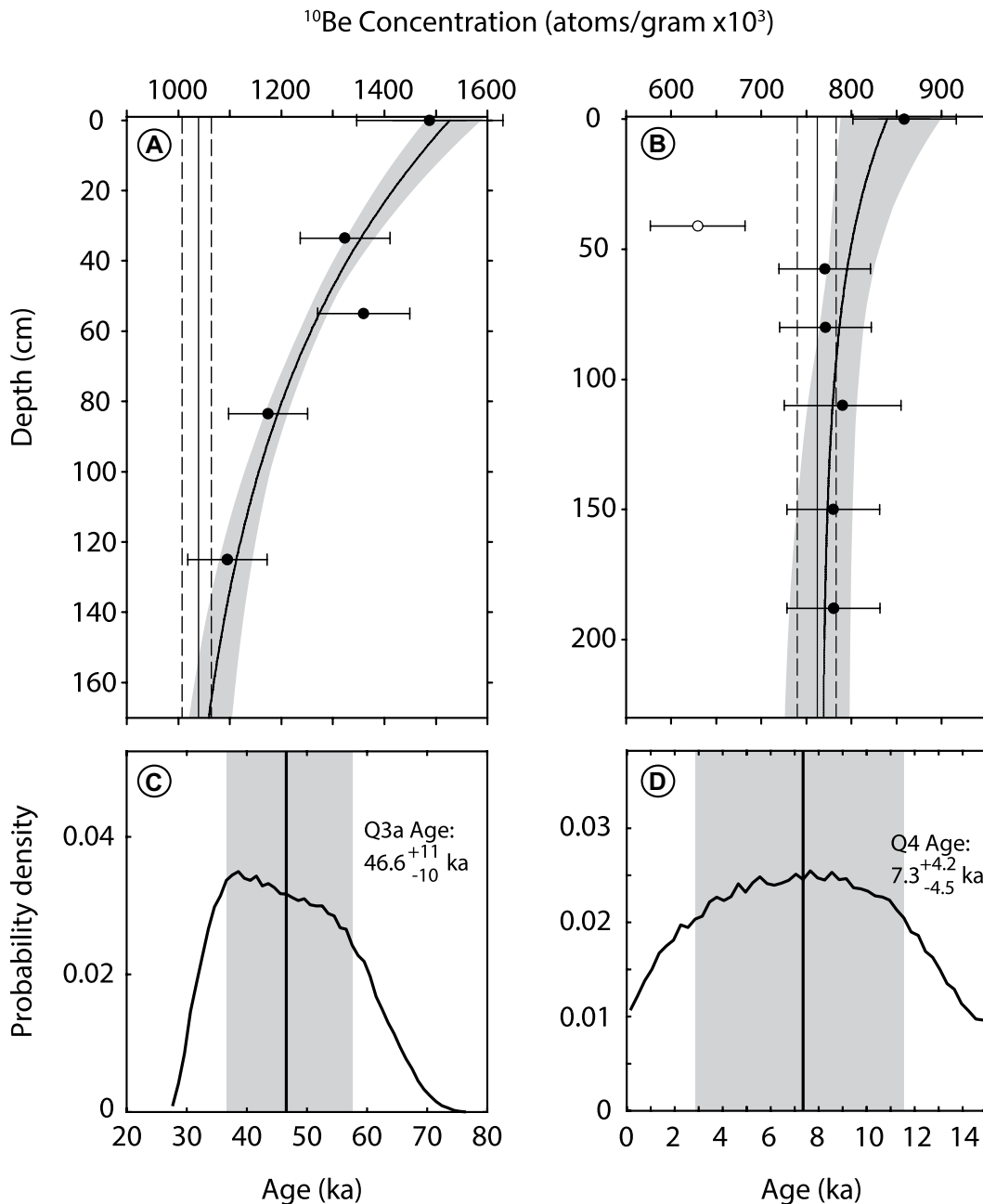
Figure 6. (A–B) [10]Be depth profile models and (C–D) exposure age probability density functions from Q3a and Q4 fan surfaces. Circles are [10]Be concentrations; horizontal error bars are the total 2σ uncertainties accounting for errors in both preparation and measurement. Filled black circles were used in the model solutions; hollow circles were excluded from model solutions. Solid black curve is the best fit to the 2σ uncertainties about each sample from the Hidy et al. (2010) Monte Carlo simulation; gray envelope in A and B is the 2σ uncertainty range of model fits. Vertical solid line represents the best-fit inheritance value, and dashed vertical lines are the 1σ uncertainty range for inheritance. The vertical gray envelope in C and D is the 1σ uncertainty about the median age.

optimum displacement measurement to visually evaluate a reasonable range of displacement. Results from LaDiCaoz displacement measurements can be found in Figures S4, S5, S6, S7, S8, and S9 of the supplemental online material.

At the Estates site, the White Mountains fault zone displaces the Q3a and Q4 alluvial fans. The Q3a surface is deeply incised by three southwest-flowing channels, and these channel walls provide robust offsets for measuring fault displacement (e.g., Gold and Cowgill, 2011; Gold et al., 2011, 2017; Mériaux et al., 2012). Here, four fault strands (F1, F2, F3, and F4) cut the Q3a fan (Figs. 5, 8, and 9); however, offset mark-

ers are only preserved along two strands (F1 and F2). We measured three channels incised into the Q3a fan that are right-laterally displaced by 36 ± 10 m (Q3a offset 1), 44 ± 10 m (Q3a offset 2), and 27 ± 8 m (Q3a offset 3; Figs. 5, 8, and 9). The Q3a offset 1 (36 ± 10 m) occurs where a previously continuous, northwest-facing channel wall has been right-laterally offset along fault strand F2, and the fan on the eastern side of the fault has been partially buried by younger Q3b fan deposits. The eastern channel wall remains exposed above the Q3b deposits and can be restored back to its original position. The uncertainty of this measurement is due to partial

burial and possible lateral erosion of the eastern channel wall (Fig. 9A; Fig. S4). The Q3a offset 2 (44 ± 10 m) occurs where a southeast-facing channel wall has been displaced along fault strand F2, leaving a downstream-facing scarp that has been shielded from erosion (Figs. 5, 8, and 9A; Fig. S5). Diffusive processes have deposited some material in the shielded corner behind the scarp, but the scarp is clearly expressed, and the projection of the unaltered channel wall into the scarp is also clear. On the south side of the channel, the northwest-facing channel wall was displaced such that an upstream-facing scarp was formed on the west side of the fault
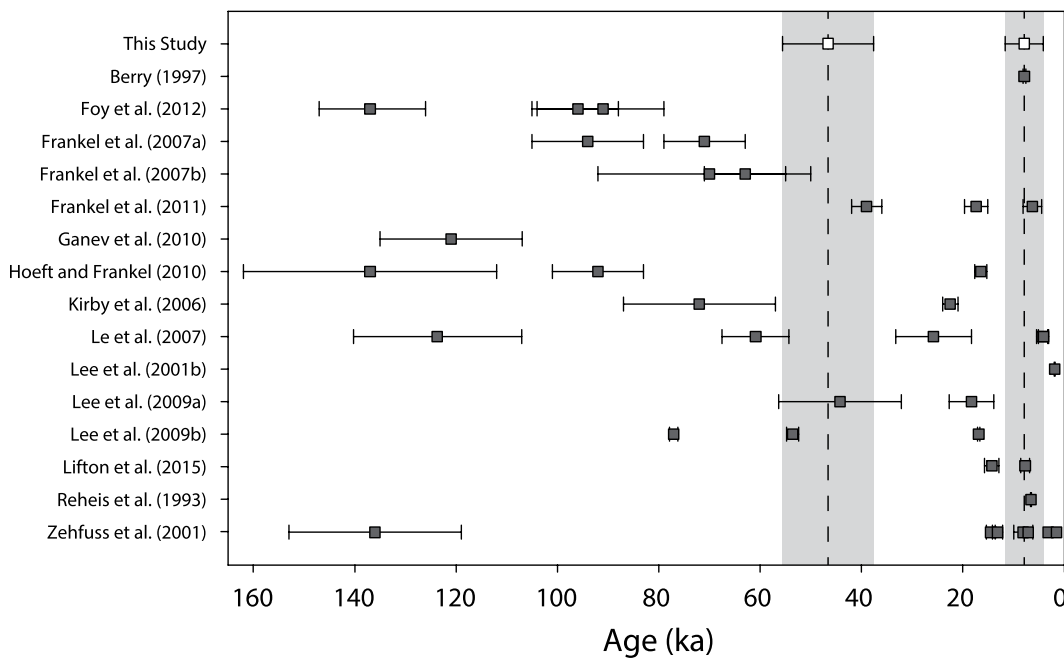
Figure 7. Ages from this study (white squares) compared to selected alluvial-fan ages and uncertainties reported in the Eastern California shear zone, Walker Lane, and Death Valley region (black squares). Dashed vertical lines correspond to our ages, and the gray shaded regions correspond to the 1σ uncertainties associated with those ages. Note that some of these ages were calculated from cosmogenic nuclide exposure using a larger production rate than the production rate used for our ages. We report the ages as published. Figure is updated and modified from Lifton et al. (2015).

and was likely quickly eroded away (Figs. 5, 8, and 9A; Fig. S5). The Q3a offset 3 (27 ± 8 m) also occurs where an offset southeast-facing channel wall has created a downstream-facing shielded scarp (Fig. 9B; Fig. S6). The Q3a offset 3 is displaced along two fault strands, F1 and F2. The total displacement of 27 ± 8 m (Fig. S6) is the sum of 6 ± 2 m of offset on fault strand F2 (Fig. S7) and 21 ± 8 m of offset on fault strand F1 (Fig. S8).

The displacement on each fault strand is additive, and we chose the largest observed offset on each fault strand to sum together. We chose the largest observed offset (offset 2) because the geomorphic configuration at this site is such that erosion of channel wall markers could reduce the magnitude of observed offset, but it could not increase the observed magnitude of offset. For this reason, and because some of the mapped fault strands do not preserve evidence for measurable displacements, the displacement measurement across the fault zone is a minimum. At offset 1, the channel wall on the west side of the fault could erode south and decrease the magnitude of the offset. At offset 2, the channel wall on the west side of the fault is shielded from significant erosion, but the channel wall on the east side of the fault is exposed to active erosion in the incised channel and can more readily erode north, making the magnitude of offset smaller. Therefore, the true offset of a landform must be at least as large as the largest observed offset. Reitman et al. (2019) used landscape evolution simulations to show that many offset channels underestimate true slip. Thus, our estimate of the minimum displacement of the Q3a fan is 44 ± 10 m

(on fault strand F2) plus 21 ± 8 m (on fault strand F1), or a total of 65 ± 13 m. We treated displacement measurements as a Gaussian distribution because the primary measurement is our preferred reconstruction of geomorphic markers, and the upper and lower confidence bounds are possible but less likely. As such, the uncertainties are added in quadrature (i.e., the square root of the sum of squares). Our estimate of uncertainty for this measurement was dictated by our ability to locate the channel walls, and by the range of displacement that allowed a reasonable reconstruction of the channel wall.

An incised ephemeral stream channel records right-lateral displacement of the Q4 fan (Figs. 5, 8, and 9C; Fig. S9). The offset occurs near the bifurcation of the fault into two subparallel strands. The fault is expressed as a small (~1-m-high) west-facing scarp in the Q4 alluvial fan. We used the thalweg of the deflected stream channel to determine total Q4 fan displacement of 14 ± 5 m. The uncertainty of this measurement is based on the natural curvature of the stream meander, which may enhance the appearance of displacement. Because the stream channel on both sides of the fault is still intact and unaltered, and a reconstruction of the original channel can be visualized, we believe that this displacement is a true measurement and not a minimum measurement.

SLIP RATES

We calculated right-lateral fault slip rates using the methods of Zechar and Frankel (2009), in which ages and displacements are treated as

PDFs. This probabilistic approach explicitly propagates the uncertainty of each measurement through the slip rate calculation. We treated the Q3a and Q4 displacement measurements as Gaussian PDFs because they consist of a preferred measurement that we believe is more likely than the upper and lower uncertainty bounds. The Q3a and Q4 age PDFs produced by the Hidy et al. (2010) model were asymmetric, so we treated those as arbitrary PDFs in the Zechar and Frankel (2009) model. The full displacement and age PDFs are shown in Figure 10, and the mode, mean, and median slip rates are tabulated in Table S1 of the supplementary data. We report the median slip rate and the 1σ uncertainty about the median, as suggested by Bird (2007) and Zechar and Frankel (2009). Any single measure of central tendency (i.e., the center point in a data set; median, mean, and mode are the most common measures of central tendency) is a simplification. The full PDF is the best way to describe a slip rate.

For a symmetric PDF, the median, mean, and mode are the same. However, these parameters diverge for asymmetric PDFs. Bird (2007) noted that in cases of right-skewed PDFs, as is the case for many slip rates, mode < median < mean. The median is a useful measure of central tendency because it is not strongly affected by outlying data points. For a highly skewed PDF, the mean will be a poor representation of central tendency because values far out on the tail of the curve skew the mean. The mode describes the peak of a PDF, but it is not necessarily a unique value, for example, with multimodal PDFs or uniform (i.e., "boxcar") distributions. While defining a

Present Day
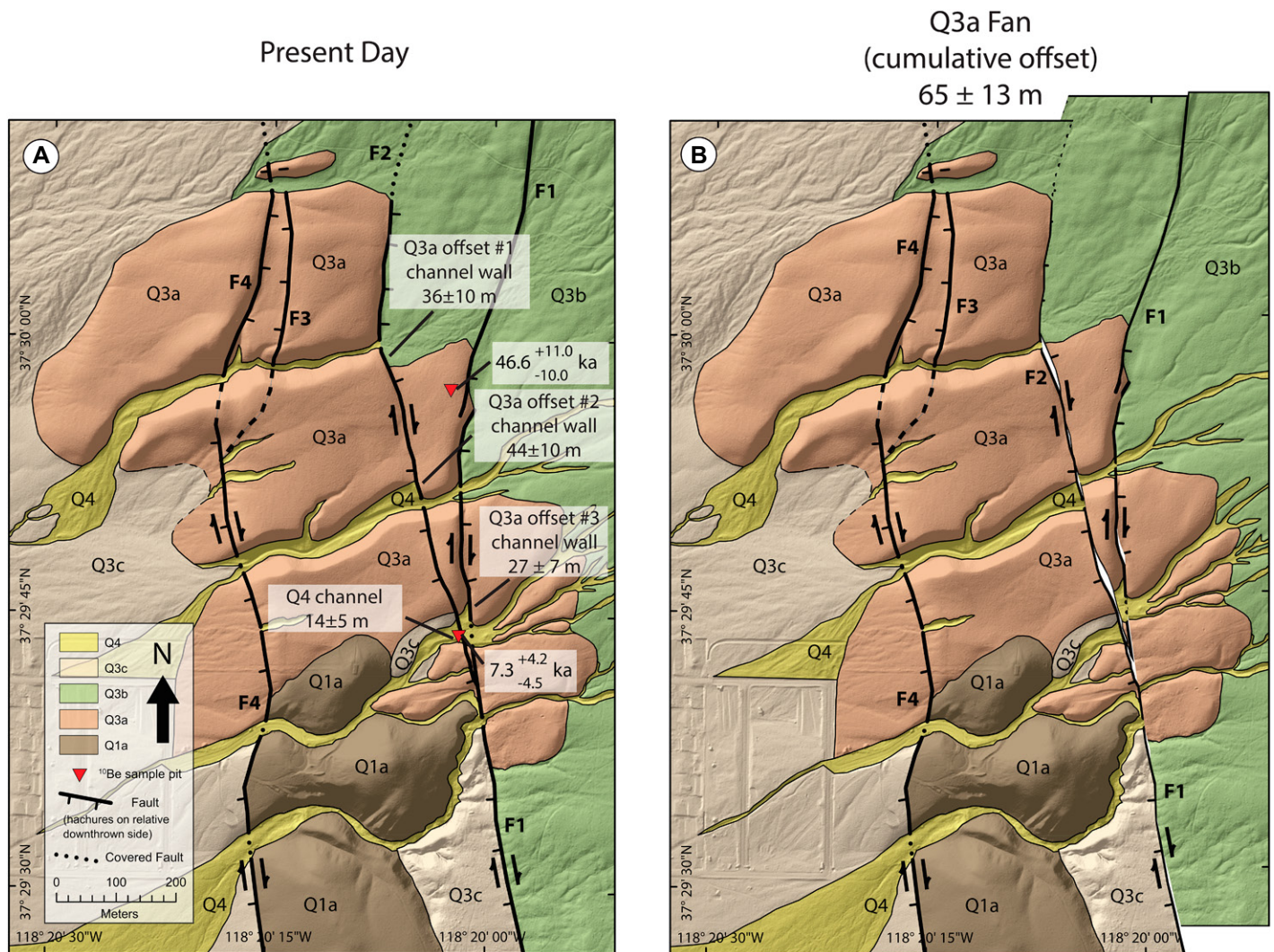
Q3a Fan
(cumulative offset)
65 ± 13 m

Figure 8. (A–B) Comparison of present-day geologic map of displaced alluvial fans at the Estates site (A) to backslipped geologic map showing restored Q3a alluvial-fan surface (B). The Q3a alluvial-fan surface is displaced a total of 65 ± 13 m by two strands of the White Mountains fault zone (see Figs. S4, S5, S6, S7, and S8 for details of Q3a offset measurements [text footnote 1]). A small abandoned channel in the Q4 fan surface is offset 14 ± 5 m (see Fig. S9 for details of Q4 offset measurement [text footnote 1]).

confidence interval about the median is straight-forward (e.g., a 95% confidence interval is bounded by values where the cumulative distribution function [CDF] reaches 0.025 and 0.975), there is not a simple way to define a confidence interval about the mode because the mode could potentially fall outside the confidence interval in cases of PDFs with very long tails. Our Q4 slip rate PDF (Fig. 9F) is an example where the right-hand tail is long enough that the lower uncertainty bound (where the CDF reaches 0.016) is almost at the mode (peak of the curve). Thus, the median has the advantages of being unique, easily bound by uncertainties, and less affected by outliers or skew. Bird (2007) preferred to report the median when only a single value can be chosen from a probability distribution. Zechar and

Frankel (2009) suggested that age, displacement, and slip rate estimates be reported as the median value with explicitly defined uncertainty bounds, and that the full probability distributions be published. These criteria for reporting slip rate data have been adopted by others in the field, e.g., Gold and Cowgill (2011). Following the suggestions of Bird (2007) and Zechar and Frankel (2009), and maintaining consistency with others in the field of active tectonics, we report the median and the 1σ uncertainty about the median. In addition, we provide the full PDFs for our ages, displacements, and slip rates as supplemental data files.

Using the displacements and ages described above, we calculated right-lateral slip rates of 1.4 + 0.5/–0.4 mm/yr and 1.9 + 2.9/–0.8 mm/

yr along the White Mountains fault zone since abandonment of the Q3a and Q4 fan surfaces, respectively (Fig. 10; Table 3). When estimating slip rates on faults cutting alluvial fans, we made three important assumptions: (1) The upper ~2 m section of the alluvial fan was deposited rapidly over a short period of time (within a few thousand years); (2) accumulation of TCNs began at the time of deposition; and (3) the fault displaced the alluvial fan soon after it was deposited, isolating the fan surface from further deposition and allowing it to be preserved. In other words, the exposure age of the fan is a maximum age for fault offset, since it is possible the fault offset the fan long after the fan was abandoned.

The slip rates presented here are minima for at least three reasons: (1) Fan exposure ages are
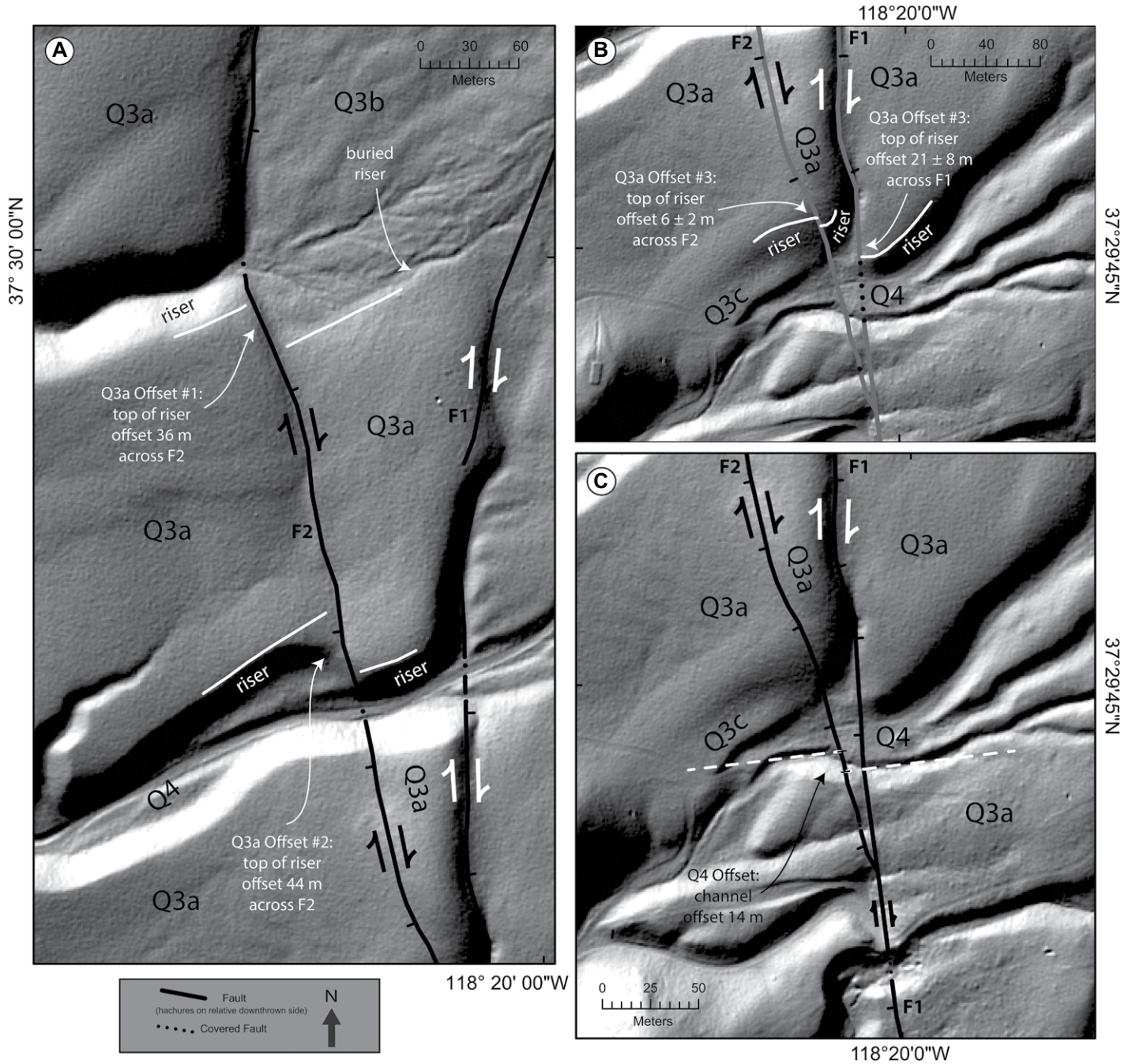
Figure 9. (A–C) Detailed maps showing the interpretation and measurement of (A) Q3a offsets 1 and 2, (B) Q3a offset 3, and (C) Q4 offset. Panel B shows that the channel wall (Q3a offset 3) has been offset by two fault strands, F1 (21 ± 8 m) and F2 (6 ± 2 m), for a total offset of 27 ± 8 m. Base map is a hillshade derived from 2012 airborne light detection and ranging (LiDAR) topographic data (Lifton, 2012). Hillshade illumination is from 315° azimuth and 45° elevation. Solid white lines mark the top of fan surface risers along incised channels. Dashed white line in C is the projection of channel orientation on either side of the fault.

maxima because we assumed that displacement of alluvial fans occurred shortly after deposition, but displacement may have occurred any time after deposition; (2) displacement measurements are minima because offset markers were not observed on all strands of the fault, and therefore we cannot account for all the displacement across the entire White Mountains fault zone; and (3) displacement measurements are minima because the geomorphic configuration at this site is such that erosion of channel walls could reduce the magnitude of observed offset, but it could not increase the observed magnitude of offset.

Because the Q3a and Q4 slip rates overlap in time (both cover the time period from 7.3 ka to present), are the same within uncertainty, and were calculated from nearby locations on the same fault, we combined them to yield a single average slip rate. We fit a linear regression to our two slip rates and the origin using

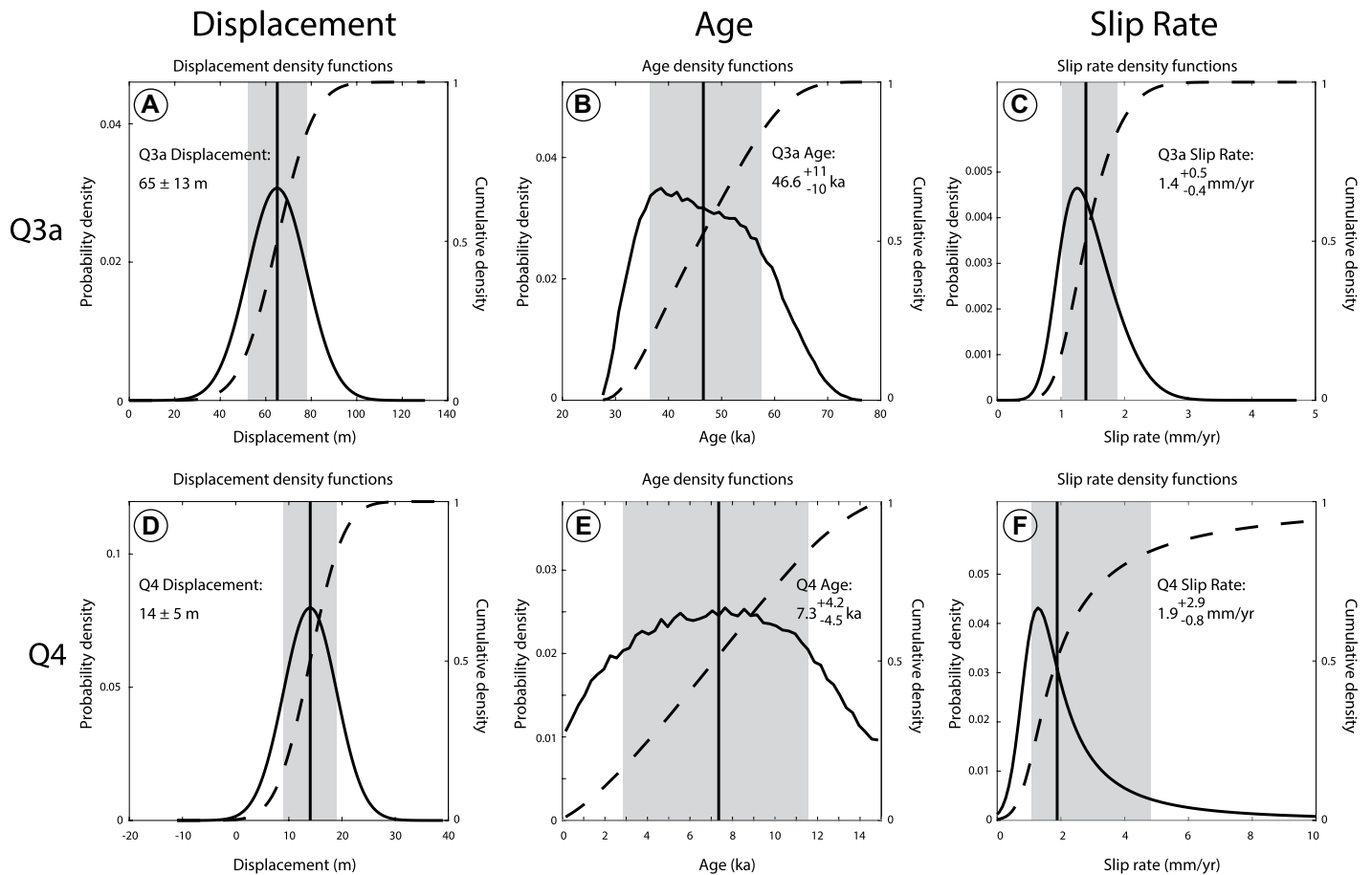## Displacement

Age

Slip Rate

Figure 10. Full probability distributions for displacement, age, and calculated slip rates. Black curves are the probability density functions; dashed lines are the cumulative density functions. Vertical black lines are median values; gray shaded areas are 1σ uncertainties about the median.

the York-Williamson method (Cantrell, 2008) to fit data with *x* and *y* uncertainties (1σ uncertainties about the median). We included the origin, which represents zero displacement and zero age, because the fault is currently in an open interval between the last known displacement and the next displacement. The linear regression yielded an average right-lateral slip rate of 1.4 ± 0.3 mm/yr for the White Mountains fault zone during the late Pleistocene and Holocene (Fig. 11).

DISCUSSION

Dextral slip along the White Mountains fault zone has been linked to dextral slip along the Owens Valley fault via a set of northeast-striking normal faults located in northern Owens Valley (e.g., Lee et al., 2001a; Sheehan, 2007). Along the Owens Valley fault, slip rate estimates vary from ~0.6 to 4.5 mm/yr during the late Pleistocene and Holocene (Lee et al., 2001a; Kirby et al., 2008; Haddon et al., 2016). Thus, if slip from the Owens Valley fault continues north onto the White Mountains fault zone (e.g., Lee

et al., 2001a; Sheehan, 2007), slip rates on the two faults over similar time scales should be similar. However, Kirby et al. (2006) previously estimated a late Pleistocene slip rate on the White Mountains fault zone of 0.3–0.4 mm/yr, which represents only ~7%–67% of the right-lateral slip rate along the Owens Valley fault, and DeLano et al. (2019) hypothesized that Owens Valley fault slip was partitioned into two components, one component northeastward onto the White Mountains fault zone and one component northwestward into the Volcanic Tableland. We tested the hypothesis that slip is transferred from the Owens Valley fault to the White Mountains

fault zone by estimating new late Pleistocene and Holocene slip rates on the White Mountains fault zone at a new site. Kirby et al. (2006) used the age (22.5 ± 1.5 ka) and offset (8 ± 1 m) of a laterally displaced boulder levee at the mouth of Sabies Canyon to calculate a late Pleistocene right-lateral slip rate of 0.3–0.4 mm/yr. Our depth profile results suggest that there is a relatively large component of inheritance in the Q3a and Q4 fan deposits. Therefore, we speculate that boulders Kirby et al. (2006) sampled for their 22.5 ± 1.5 ka age fan, which were derived from an unglaciated basin, may have contained inherited cosmogenic nuclides that resulted in

TABLE 3. OFFSET ALLUVIAL-FAN EXPOSURE AGES AND SLIP
RATES ALONG WHITE MOUNTAINS FAULT ZONE

Alluvial-fan deposit	Magnitude of offset* (m)	Direction of slip (degrees)	Median age and 1σ uncertainty (ka)	Calculated minimum slip rate (mm/yr)	Slip rate projected toward 323°† (mm/yr)
Q3a	65 ± 13	350	46.6 + 11.0/–10.0	1.4 + 0.5/–0.4	1.2 ± 0.4
Q4	14 ± 5	350	7.3 + 4.2/–4.5	1.9 + 2.9/–0.8	1.7 + 2.6/–0.7

*Minimum offset magnitude due to lack of offset markers on all mapped fault strands.
†Slip rate projected parallel to Sierra Nevada–Great Valley (SNGV) and Central Great Basin (CGB) plate motion of 323° (Bennett et al., 2003).
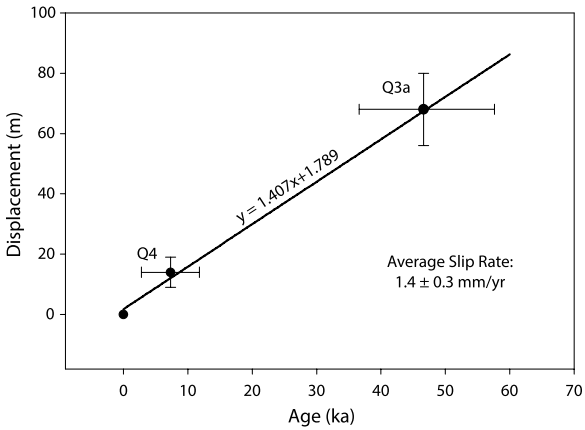
Figure 11. Plot of age vs. displacement for the offset Q3a and Q4 fans. Error bars in the *x* and *y* directions represent 1σ uncertainties about the median. A third data point, at zero displacement and zero age (present), is included because the fault is currently in an open interval between the last known displacement and the next displacement. A linear regression was fit to the points using the York-Williamson method described by Cantrell (2008), which accounts for uncertainty of both age and displacement.

boulder ages older than the true exposure age, ultimately yielding an artificially low slip rate. That study suggested that a major change in the local stress field sometime before ca. 70 ka caused slip rates on the White Mountains fault zone to slow dramatically. Our results suggest that the White Mountains fault zone slip rate during the late Pleistocene and Holocene was significantly faster, at 1.4 ± 0.3 mm/yr, than previously reported, but they do not help answer the question of slip rate changes since the middle Pleistocene.

We documented two right-lateral slip rates spanning the late Pleistocene through the Holocene that suggest the slip rate on the White Mountains fault zone is faster than previously reported. As discussed above, our ~1.4–1.9 mm/yr dextral slip rate estimates are minima. These slip rates are consistent with either all of Owens Valley fault slip transferred to the White Mountains fault zone or partitioning of Owens Valley fault slip into two components, one component transferred northeastward onto the White Mountains fault zone and another transferred northwestward into the Volcanic Tableland (e.g., Nagorsen-Rinke et al., 2013; DeLano et al., 2019).

Our results have implications for long- versus short-term slip rates across the Walker Lane. At ~36.5°N latitude, the sum of long-term geologic slip rates is the same, within error, to the short-term geodetic slip rates (cf. Bennett et al., 2003; Lee et al., 2009a). In contrast, there has been a significant discrepancy observed in the southern Walker Lane at ~37.5°N latitude between long-term geologic slip rates and short-term geodetic slip rates. The sum of published middle to late Pleistocene slip rates along transect A-A′ (Fig. 2), projected toward the Sierra Nevada–Great Valley and Central Great Basin relative motion direction of 323°, across this part of the Walker Lane is 7.4 + 1.2/–0.6 mm/yr

(Table 1; Kirby et al., 2006; Frankel et al., 2011; Reheis and Sawyer, 1997; Foy et al., 2012; Lifton et al., 2015; DeLano et al., 2019). However, dislocation models constrained by GPS data predict a long-term slip rate at ~37.5°N latitude of 10.6 ± 0.5 mm/yr along the same transect (Lifton et al., 2013). Many hypotheses have been invoked to explain this discrepancy, including transient strain (Frankel et al., 2011), postseismic relaxation following the 1872 magnitude (M) 7.6 Owens Valley earthquake (Hammond et al., 2009; Dixon et al., 2003), distributed strain across the region (Frankel et al., 2011; Foy et al., 2012; Nagorsen-Rinke et al., 2013), or underestimation of true slip rates from minimum late Pleistocene normal and/or dextral fault slip rate

estimates across the southern Walker Lane (DeLano et al., 2019). Including our new average late Pleistocene slip rate estimate of 1.4 ± 0.3 mm/yr for the White Mountains fault zone brings the sum of slip across this part of the Walker Lane toward 323° to 7.9 + 1.3/–0.6 mm/yr, or ~75% of the predicted geodetic slip rate (Fig. 12).

We considered several hypotheses to account for the remaining difference between long- and short-term slip rates. First, since our fault slip rates, and those published by others, are minima, the long- versus short-term discrepancy could potentially be resolved if geologic slip rates were slightly higher than reported minima, a hypothesis in line with that of DeLano et al. (2019). Slip rates may be higher than reported minima in cases where alluvial-fan offset is larger (e.g., where we mapped additional fault strands that do not preserve evidence for measurable dextral offset), or where the interval of time over which the rate is calculated is shorter (e.g., if initiation of displacement occurred long after an alluvial-fan surface was abandoned).

Second, some proportion of strain may be accommodated off of primary faults in a distributed fashion. This may result in deformation that is unrecognized because it is too small to rupture the surface or because small surface ruptures that occur in unconsolidated basin fill are not preserved in the landscape. For example, the 1986 M 6.2 Chalfant earthquake on the White Mountains fault zone caused minor ground fracturing both on and off of previously mapped fault traces along the White Mountains range front and across the valley in the Volcanic Tableland,
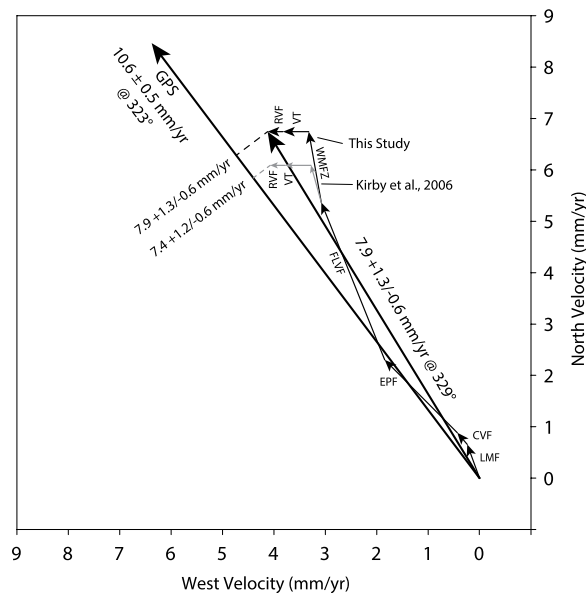

Figure 12. Velocity vector diagram for the southern Walker Lane comparing short-term geodetic slip rates to long-term geologic slip rates. The total slip rate measured by global positioning system (GPS) is 10.6 ± 0.5 mm/yr toward an azimuth of 323° (Lifton et al., 2013). Two values for the White Mountains fault zone (WMFZ) are plotted from the end of the Fish Lake Valley fault (FLVF) vector: the previously published rate estimated by Kirby et al. (2006; small gray arrows), and the results from this study. The sum of the slip rates is projected toward an azimuth of 323° (dashed lines). See Table 1 for slip rate data used in this diagram. RVF—Round Valley fault, VT—Volcanic Tableland, EPF—Emigrant Peak fault, CVF—Clayton Valley fault, LMF—Lone Mountain fault.

but it did not leave a long-term record of rupture (Lienkaemper et al., 1987). Distributed deformation has been proposed as a possible source of uncertainty in geologic slip rates (e.g., Foy et al., 2012; Zinke et al., 2014; Gold et al., 2015; Milliner et al., 2015; Graveleau et al., 2015; Reitman et al., 2019) and has potential to account for as much as ~45% of total strain. Distributed deformation is difficult to quantify, but future applications of high-resolution LiDAR data may provide a means to estimate the proportion of strain occurring away from major faults.

Third, slip may be accommodated within Owens Valley and further west across the Fish Slough fault, the Volcanic Tableland, the Round Valley fault, or other faults as hypothesized by Nagorsen-Rinke et al. (2013) and DeLano et al., (2019). This westward routing would allow for transfer of a portion of Owens Valley fault slip into the Adobe Hills, located in the southwestern part of the Mina Deflection (Nagorsen-Rinke et al., 2013; DeLano et al., 2019). While right-lateral slip rates are not well documented on these faults, evidence suggests they may be accommodating right-lateral displacement. Specifically, the 1986 M 6.2 Chalfant earthquake and 1986 M 5.2 White Mountains earthquake caused minor right-lateral surface fractures, and the seismicity and fault plane surface projection trend north-northwest from the White Mountains range front toward the Volcanic Tableland (Lienkaemper et al., 1987; dePolo, 1989; Stockli et al., 2003). Bateman (1965) suggested that the en echelon geometry of faults across the Volcanic Tableland and adjacent broad folds were the result of right-lateral shear. In addition, Nagorsen-Rinke et al. (2013) made two important observations: (1) most of the normal faults across the Volcanic Tableland strike clockwise (more northerly) with respect to the relative motion between the Sierra Nevada and North America, thus defining releasing steps in a right-lateral slip system, and (2) some of the normal faults curve into parallelism with Sierra Nevada and North America relative motion, implying they record a right-lateral component of slip. DeLano et al. (2019) proposed two models for the transfer of right-lateral slip north of the Owens Valley fault. In the first model, slip is partitioned between the White Mountains fault zone (2.7 mm/yr) and extension across the Volcanic Tableland (0.4 mm/yr). In the second model, slip is partitioned among the White Mountains fault zone (1.9 mm/yr), extension across the Volcanic Tableland (0.5 mm/yr), and right-lateral slip on the Round Valley fault along the Sierra Nevada range front (0.8 mm/yr). In either case, the models of DeLano et al. (2019) require slip to be transferred to the west of the White Mountains fault zone. These models are consistent with

geodetic measurements suggesting that ~2 mm/yr of right-lateral deformation is being accommodated between the White Mountains and the Sierra Nevada range (Dixon et al., 2000; McCaffrey, 2005; Lifton et al., 2013).

A fourth hypothesis to explain the slip discrepancy is that fault slip is transferred from the relatively narrow zone of deformation along the Fish Lake Valley fault northeast into a broader, distributed zone of deformation that defines the Silver Peak–Lone Mountain extensional complex (e.g., Frankel et al., 2011). Extension on the Silver Peak–Lone Mountain normal faults is approximately parallel to the direction of shear in the Walker Lane. The Silver Peak–Lone Mountain extensional complex may act as an extensional step-over structure (e.g., Oldow et al., 1994; Dixon et al., 1995; Reheis and Dixon, 1996), in much the same way as the Queen Valley fault (Lee et al., 2009b), Deep Springs fault (Lee et al., 2001b), and Tin Mountain fault (Fig. 2). The Silver Peak–Lone Mountain extensional complex provides a potential route for strain to transfer from the southern Walker Lane to the central Walker Lane, bypassing the Mina Deflection and transferring strain between the Fish Lake Valley fault and the Benton Spring, Petrified Springs, and Monte Cristo right-lateral faults to the northeast. Evidence of distributed deformation across the Silver Peak–Lone Mountain extensional complex (e.g., Foy et al., 2012; Christie et al., 2009) suggests that the extensional zone might be accommodating more strain than is documented. Furthermore, there is evidence for accelerating extension across the Silver Peak–Lone Mountain complex (Reheis and Sawyer, 1997; Hoeft and Frankel, 2010; Lifton et al., 2015), implying that this region may be an important region for accommodating strain in the southern Walker Lane. Additional right-lateral strain may be accommodated east of Lone Mountain (Fig. 2), at the eastern edge of the Walker Lane on the north-striking San Antonio fault (DeLano et al., 2019). While the San Antonio fault has not been studied in detail, Pérouse and Wernicke (2017) suggested that similar Basin and Range faults have late Pleistocene slip rates of ~0.2–0.3 mm/yr, which, if projected to 323° and included in the sum of slip rates, would only contribute ~0.1 mm/yr of slip.

CONCLUSIONS

We presented new geologic mapping, high-resolution LiDAR data, and [10]Be TCN exposure dates to estimate two right-lateral slip rates on the White Mountains fault zone spanning the late Pleistocene to Holocene. Alluvial fans with ages of 46.6 + 11.0/–10.0 ka and 7.3 + 4.2/–4.5 ka have been right-laterally displaced by a mini-

mum of 65 ± 13 m and 14 ± 5 m, respectively, yielding minimum average geologic slip rates of 1.4 + 0.5/–0.4 mm/yr (since deposition of surface Q3a) and 1.9 + 2.9/–0.8 mm/yr (since deposition of surface Q4). The average of these two slip rates over the past ~46 k.y. is 1.4 ± 0.3 mm/yr. These results have implications for the constancy of slip by helping account for some of the discrepancy between long- and short-term slip rates. Our results suggest that slip rates on the White Mountains fault zone are faster than previously reported, and therefore the White Mountains fault zone may represent a higher seismic hazard than previously assumed. These new slip rates, when added to previously published rates across the southern Walker Lane at ~37.5°N latitude, sum to 7.9 + 1.3/–0.6 mm/yr of slip directed toward 323°. This accounts for ~75% of the observed geodetic slip rate of 10.6 ± 0.5 mm/yr (Lifton et al., 2013). We hypothesize that the remaining "missing" slip may be accommodated: (1) on existing primary faults, if true geologic slip rates are greater than the published minimum geologic slip rates; (2) in a distributed fashion off the major right-lateral faults in this part of the Walker Lane; (3) to the west of the White Mountains fault zone in the Volcanic Tableland and faults on the eastern side of the Sierra Nevada; and/or (4) to the east of the Fish Lake Valley fault via accelerating extension of the Silver Peak–Lone Mountain complex.

APPENDIX A: ALLUVIAL-FAN UNIT DESCRIPTIONS

Q1a Alluvial-Fan Unit

Q1a surfaces are highly dissected into a ridge-and-ravine morphology. The degree of dissection ranges from a few meters to tens of meters. Q1a surfaces appear light in color in aerial photographs due to the lack of rock varnish. In some localities, desert pavement remnants exist on the apex of ridges, but diffusive processes have degraded them. Soils within Q1a units generally have a 4–5-cm-thick Av horizon immediately below the surface. Below the Av horizon, pebble- to cobble-sized grains have thick pedogenic carbonate coatings. Carbonate stringers appear throughout the soil profile. This alluvial-fan unit may correlate to the Qsco (older alluvium of Silver Canyon) unit of Kirby et al. (2006).

Q3a Alluvial-Fan Unit

The Q3a alluvial-fan surface is planar, with no distinguishable bar-and-swale topographic relief. A moderately interlocking desert pavement of cobble- and gravel-sized clasts has developed on this surface. Clasts are moderately varnished and rubified, and they are composed of fine-grained metasedimentary rock, limestone, and vein quartz. The surface is ~10–15 m above the modern stream channel. Moderately developed pedogenic carbonate coatings occur on some clasts throughout the deposit, but they are thickest between 60 cm and 120 cm depth. The deposit is moderately cemented between 60 cm and 120 cm depth. This alluvial-fan

unit correlates to the Qf4o (older alluvium) unit of Kirby et al. (2006).

Q3b Alluvial-Fan Units

The Q3b alluvial-fan unit is part of an extensive alluvial-fan apron deposited along the western flank of the White Mountains. The Q3b alluvial-fan surface is relatively planar. Bar-and-swale morphology is present, but very subdued, and it has <10 cm of topographic relief. The bar-and-swale surface morphology on the older Q3b surfaces is more subdued than younger Q3c surfaces. The surface is ~1–3 m above the most recently active stream channel. The surface has abundant silt and sand, with a thin veneer of non-interlocking gravel-sized clasts composed of fine-grained metasedimentary rock, vein quartz, and limestone. Desert varnish is absent or very weakly developed. Soils are weakly developed, with a 0–2-cm-thick Av horizon and occasional thin pedogenic carbonate coatings on surface clasts. This alluvial-fan unit correlates to the Qf4y (younger alluvium and debris-flow deposits) unit of Kirby et al. (2006).

Q3c Alluvial-Fan Unit

The Q3c alluvial-fan surface is relatively planar. Bar-and-swale morphology is present, but very subdued, and it has ~10 cm of topographic relief. The surface is ~1–3 m above the most recently active stream channel. The surface has abundant silt and sand, with a thin veneer of non-interlocking gravel-sized clasts composed of fine-grained metasedimentary rock, vein quartz, and limestone. Desert pavement and desert varnish are absent. Some clasts have a thin pedogenic carbonate coating; however, these may be relict coatings from previous residence of sediment in earlier fan deposits. The Q3c unit is very similar to unit Q3b; unit Q3c is distinguished by a more prominent bar-and-swale topography, and a lighter color in aerial photographs. This alluvial-fan unit may also correlate to the Qf4y (younger alluvium and debris-flow deposits) unit of Kirby et al. (2006).

Q4 Alluvial-Fan Unit and Active Channel

The Q4 alluvial-fan surface is ~1 m above the recently active channel, and it was deposited at the bottom of relict channels that incise into older, higher fan surfaces. The Q4 alluvial-fan unit consists of flat-lying deposits of abundant silt with a thin veneer of angular to subrounded gravel. The gravel lithology is primarily shale and slate, with rare clasts of vein quartz. No desert varnish or desert pavement has developed on the Q4 alluvial-fan unit. The Q4 map unit also includes the most recently active stream channel incised into the alluvial fan. These ephemeral channels typically incise or are bounded by the Q4 alluvial-fan deposits, and they are narrow and not easily distinguished at the scale of our mapping.

APPENDIX B: TCN SAMPLE PREPARATION

Samples were prepared at the Georgia Tech TCN Geochronology Laboratory following standard methods (e.g., Kohl and Nishiizumi, 1992). Depth profile samples were sieved to isolate the appropriate size fraction. The 250–500 µm size fraction is ideal for depth profile analysis, but in some cases, we expanded the range of grain size in order to retain enough material for analysis. We used the 250–710 µm size fraction for the Q3a depth profile and the 125–710 µm size fraction for the Q4 depth profile. Surface clasts

were crushed and mixed into a single amalgamation for each surface and then sieved to isolate the 250–500 µm size fraction. Quartz was isolated and purified with a series of HF leaches in heated ultrasonic tanks. After dissolution, Be was extracted from the quartz by ion exchange chromatography, then precipitated as $Be(OH)_2$, and oxidized to BeO. The BeO was mixed with niobium powder and packed in a target. The $^{10}Be/^9Be$ ratio of each sample was measured by accelerator mass spectrometry at the Center for Accelerator Mass Spectrometry at Lawrence Livermore National Laboratory (CAMS-LLNL). Isotopic ratios were normalized to standard 07KNSTD3110 with a value of 2.85×10^{-12} (Nishiizumi et al., 2007). TCN analytical data can be found in Table 2.

REFERENCES CITED

Anderson, R.S., Repka, J.L., and Dick, G.S., 1996, Explicit treatment of inheritance in dating depositional surfaces using in situ ^{10}Be and ^{26}Al: Geology, v. 24, p. 47–51, https://doi.org/10.1130/0091-7613(1996)024<0047:ETOIID>2.3.CO;2.

Bateman, P.C., 1965, Geology and Tungsten Mineralization of the Bishop District, California: U.S. Geological Survey Professional Paper 470, 208 p.

Bennett, R., Wernicke, B., Niemi, N., Friedrich, A., and Davis, J., 2003, Contemporary strain rates in the northern Basin and Range Province from GPS data: Tectonics, v. 22, 1008, https://doi.org/10.1029/2001TC001355.

Berry, M.E., 1997, Geomorphic analysis of late Quaternary faulting on Hilton Creek, Round Valley and Coyote Warp faults, east-central Sierra Nevada, California, USA: Geomorphology, v. 20, p. 177–195, https://doi.org/10.1016/S0169-555X(97)00033-0.

Bird, P., 2007, Uncertainties in long-term geologic offset rates of faults: General principles illustrated with data from California and other western states: Geosphere, v. 3, no. 6, p. 577–595, https://doi.org/10.1130/GES00127.1.

Borchers, B., Marrero, S., Balco, G., Caffee, M., Goehring, B., Lifton, N., Nishiizumi, K., Phillips, F., Schaefer, J., and Stone, J., 2016, Geological calibration of spallation production rates in the CRONUS-Earth project: Quaternary Geochronology, v. 31, p. 188–198, https://doi.org/10.1016/j.quageo.2015.01.009.

Bull, W.B., 1991, Geomorphic Responses to Climatic Change: New York, Oxford University Press, 352 p.

Cantrell, C.A., 2008, Review of methods for linear least-squares fitting of data and application to atmospheric chemistry problems: Atmospheric Chemistry and Physics, v. 8, p. 5477–5487 https://www.atmos-chem-phys.net/8/5477/2008/, https://doi.org/10.5194/acp-8-5477-2008.

Christie, M., Tsoflias, G.P., Stockli, D.F., and Black, R., 2009, Assessing fault displacement and off-fault deformation in an extensional tectonic setting using 3-D ground-penetrating radar imaging: Journal of Applied Geophysics, v. 68, no. 1, p. 9–16, https://doi.org/10.1016/j.jappgeo.2008.10.013.

Cowgill, E., Gold, R.D., Xuanhua, C., Xiao-Feng, W., Arrowsmith, J.R., and Southon, J., 2009, Low Quaternary slip rate reconciles geodetic and geologic rates along the Altyn Tagh fault, northwestern Tibet: Geology, v. 37, p. 647–650, https://doi.org/10.1130/G25623A.1.

Crowder, D.F., McKee, E.H., Ross, D.C., and Krauskopf, K.B., 1973, Granitic rocks of the White Mountains area, California-Nevada: Age and regional significance: Geological Society of America Bulletin, v. 84, p. 285–296, https://doi.org/10.1130/0016-7606(1973)84<285:GROTWM>2.0.CO;2.

DeLano, K., Lee, J., Roper, R., and Calvert, A., 2019, Dextral, normal, and sinistral faulting across the Eastern California shear zone–Mina deflection transition, California-Nevada, USA: Geosphere, v. 15, p. 1206–1239, https://doi.org/10.1130/GES01636.1.

DeMets, C., Gordon, R.G., and Argus, D.F., 2010, Geologically current plate motions: Geophysical Journal International, v. 181, no. 1, p. 1–80, https://doi.org/10.1111/j.1365-246X.2009.04491.x.

dePolo, C.M., 1989, Seismotectonics of the White Mountains Fault System, East-Central California and West-Central Nevada [M.S. thesis]: Reno, Nevada, University of Nevada, 354 p.

dePolo, C.M., and Ramelli, A.R., 1987, Preliminary report on surface fractures along the White Mountains fault zone associated with the July 1986 Chalfant Valley earthquake sequence: Bulletin of the Seismological Society of America, v. 77, p. 290–296.

Dixon, T.H., Robaudo, S., Lee, J., and Reheis, M.C., 1995, Constraints on present-day Basin and Range deformation from space geodesy: Tectonics, v. 14, p. 755–772, https://doi.org/10.1029/95TC00931.

Dixon, T.H., Miller, M., Farina, F., Wang, H., and Johnson, D., 2000, Present-day motion of the Sierra Nevada block and some tectonic implications for the Basin and Range Province, North America: Tectonics, v. 19, p. 1–24, https://doi.org/10.1029/1998TC001088.

Dixon, T.H., Norabuena, E., and Hotaling, L., 2003, Paleoseismology and global positioning system: Earthquake-cycle effects and geodetic versus geologic fault slip rates in the Eastern California shear zone: Geology, v. 31, p. 55–58, https://doi.org/10.1130/0091-7613(2003)031<0055:PAGPSE>2.0.CO;2.

Dolan, J.F., Bowman, D.D., and Sammis, C.G., 2007, Long-range and long-term fault interactions in Southern California: Geology, v. 35, p. 855–858, https://doi.org/10.1130/G23789A.1.

Fenneman, N.M., and Johnson, D.W., 1946, Physiographic Divisions of the Conterminous U.S.: Washington, D.C., U.S. Geological Survey, scale 1:7,000,000, https://water.usgs.gov/GIS/metadata/usgswrd/XML/physio.xml.

Foy, T.A., Frankel, K.L., Lifton, Z.M., Johnson, C.W., and Caffee, M.W., 2012, Distributed extensional deformation in a zone of right-lateral shear: Implications for geodetic versus geologic rates of deformation in the Eastern California shear zone–Walker Lane: Tectonics, v. 31, TC4008, https://doi.org/10.1029/2011TC002930.

Frankel, K.L., Brantley, K.S., Dolan, J.F., Finkel, R.C., Klinger, R.E., Knott, J.R., Machette, M.N., Owen, L.A., Phillips, F.M., Slate, J.L., and Wernicke, B.P., 2007a, Cosmogenic ^{10}Be and ^{36}Cl geochronology of offset alluvial fans along the northern Death Valley fault zone: Implications for transient strain in the Eastern California shear zone: Journal of Geophysical Research, v. 112, B06407, https://doi.org/10.1029/2006JB004350.

Frankel, K.L., Dolan, J.F., Finkel, R.C., Owen, L.A., and Hoeft, J.S., 2007b, Spatial variations in slip rate along

the Death Valley–Fish Lake Valley fault system determined from LiDAR topographic data and cosmogenic [10]Be geochronology: Geophysical Research Letters, v. 34, L18303, https://doi.org/10.1029/2007GL030549.

Frankel, K.L., Dolan, J.F., Owen, L.A., Ganev, P., and Finkel, R.C., 2011, Spatial and temporal constancy of seismic strain release along an evolving segment of the Pacific–North America plate boundary: Earth and Planetary Science Letters, v. 304, p. 565–576, https://doi.org/10.1016/j.epsl.2011.02.034.

Ganev, P.N., Dolan, J.F., Frankel, K.L., and Finkel, R.C., 2010, Rates of extension along the Fish Lake Valley fault and transtensional deformation in the Eastern California shear zone–Walker Lane belt: Lithosphere, v. 2, p. 33–49, https://doi.org/10.1130/L51.1.

Gold, R.D., and Cowgill, E., 2011, Deriving fault-slip histories to test for secular variation in slip, with examples from the Kunlun and Awatere faults: Earth and Planetary Science Letters, v. 301, p. 52–64, https://doi.org/10.1016/j.epsl.2010.10.011.

Gold, R.D., Cowgill, E., Arrowsmith, J.R., Chen, X., Sharp, W.D., Cooper, K.M., and Wang, X.F., 2011, Faulted terrace risers place new constraints on the late Quaternary slip rate for the central Altyn Tagh fault, northwest Tibet: Geological Society of America Bulletin, v. 123, no. 5/6, p. 958–978, https://doi.org/10.1130/B30207.1.

Gold, R.D., Reitman, N.G., Briggs, R.W., Barnhart, W.D., Hayes, G.P., and Wilson, D., 2015, On- and off-fault deformation associated with the September 2013 Mw 7.7 Balochistan earthquake: Implications for geologic slip rate measurements: Tectonophysics, v. 660, p. 65–78, https://doi.org/10.1016/j.tecto.2015.08.019.

Gold, R.D., Briggs, R.W., Crone, A.J., and DuRoss, C.B., 2017, Refining fault slip rates using multiple displaced terrace risers—An example from the Honey Lake fault, NE California, USA: Earth and Planetary Science Letters, v. 477, p. 134–146, https://doi.org/10.1016/j.epsl.2017.08.021.

Gosse, J.C., and Phillips, F.M., 2001, Terrestrial in situ cosmogenic nuclides: Theory and application: Quaternary Science Reviews, v. 20, p. 1475–1560, https://doi.org/10.1016/S0277-3791(00)00171-2.

Graveleau, F., Strak, V., Dominguez, S., Malavieille, J., Chatton, M., Manighetti, I., and Petit, C., 2015, Experimental modelling of tectonics-erosion-sedimentation interactions in compressional, extensional, and strike-slip settings: Geomorphology, v. 244, p. 146–168, https://doi.org/10.1016/j.geomorph.2015.02.011.

Haddon, E.K., Amos, C.B., Zielke, O., Jayko, A.S., and Bürgmann, R., 2016, Surface slip during large Owens Valley earthquakes: Geochemistry Geophysics Geosystems, v. 17, p. 2239–2269, https://doi.org/10.1002/2015GC006033.

Hammond, W.C., and Thatcher, W., 2007, Crustal deformation across the Sierra Nevada, northern Walker Lane, Basin and Range transition, western United States, measured with GPS, 2000–2004: Journal of Geophysical Research, v. 112, B05411, https://doi.org/10.1029/2006JB004625.

Hammond, W.C., Kreemer, C., and Blewitt, G., 2009, Geodetic constraints on contemporary deformation in the northern Walker Lane: 3. Central Nevada seismic belt postseismic relaxation, *in* Oldow, J.S., and Cashman, P.H., eds., Late Cenozoic Structure and Evolution of the Great Basin–Sierra Nevada Transition: Geological Society of America Special Paper 447, p. 33–54, https://doi.org/10.1130/2009.2447(03).

Hanson, R.B., Saleeby, J.B., and Fates, D.G., 1987, Age and tectonic setting of Mesozoic metavolcanic and metasedimentary rocks, northern White Mountains, California: Geology, v. 15, p. 1074–1078, https://doi.org/10.1130/0091-7613(1987)15<1074:AATSOM>2.0.CO;2.

Hidy, A.J., Gosse, J.C., Pederson, J.L., Mattern, J.P., and Finkel, R.C., 2010, A geologically constrained Monte Carlo approach to modeling exposure ages from profiles of cosmogenic nuclides: An example from Lees Ferry, Arizona: Geochemistry Geophysics Geosystems, v. 11, Q0AA10, https://doi.org/10.1029/2010GC003084.

Hoeft, J.S., and Frankel, K.L., 2010, Temporal variations in extension rate on the Lone Mountain fault and strain distribution in the Eastern California shear zone–

Walker Lane: Geosphere, v. 6, p. 917–936, https://doi.org/10.1130/GES00603.1.

Kirby, E., Burbank, D.W., Reheis, M., and Phillips, F., 2006, Temporal variations in slip rate of the White Mountain fault zone, eastern California: Earth and Planetary Science Letters, v. 248, p. 168–185, https://doi.org/10.1016/j.epsl.2006.05.026.

Kirby, E., Anandakrishnan, S., Phillips, F., and Marrero, S., 2008, Late Pleistocene slip rate along the Owens Valley fault, eastern California: Geophysical Research Letters, v. 35, L01304, https://doi.org/10.1029/2007GL031970.

Kohl, C.P., and Nishiizumi, K., 1992, Chemical isolation of quartz for measurement of in-situ–produced cosmogenic nuclides: Geochimica et Cosmochimica Acta, v. 56, p. 3583–3587, https://doi.org/10.1016/0016-7037(92)90401-4.

Krauskopf, K.B., 1971, Geologic Map of the Mount Barcroft Quadrangle, California-Nevada: U.S. Geological Survey Geologic Quadrangle Map GQ-960, scale 1:62,500.

Lal, D., 1991, Cosmic ray labeling of erosion surfaces: In situ nuclide production rates and erosion models: Earth and Planetary Science Letters, v. 104, p. 424–439, https://doi.org/10.1016/0012-821X(91)90220-C.

Le, K., Lee, J., Owen, L.A., and Finkel, R., 2007, Late Quaternary slip rates along the Sierra Nevada frontal fault zone, California: Slip partitioning across the western margin of the Eastern California shear zone–Basin and Range Province: Geological Society of America Bulletin, v. 119, p. 240–256, https://doi.org/10.1130/B25960.1.

Lee, J., Spencer, J., and Owen, L., 2001a, Holocene slip rates along the Owens Valley fault, California: Implications for the recent evolution of the Eastern California shear zone: Geology, v. 29, p. 819–822, https://doi.org/10.1130/0091-7613(2001)029<0819:HSRATO>2.0.CO;2.

Lee, J., Rubin, C.M., and Calvert, A., 2001b, Quaternary faulting history along Deep Springs fault, California: Geological Society of America Bulletin, v. 113, p. 855–869, https://doi.org/10.1130/0016-7606(2001)113<0855:QFHATD>2.0.CO;2.

Lee, J., Stockli, D.F., Owen, L.A., Finkel, R.C., and Kislitsyn, R., 2009a, Exhumation of the Inyo Mountains, California: Implications for the timing of extension along the western boundary of the Basin and Range Province and distribution of dextral fault slip rates across the Eastern California shear zone: Tectonics, v. 28, TC1001, https://doi.org/10.1029/2008TC002295.

Lee, J., Garwood, J., Stockli, D.F., and Gosse, J., 2009b, Quaternary faulting in Queen Valley, California-Nevada: Implications for kinematics of fault-slip transfer in the Eastern California shear zone–Walker Lane belt: Geological Society of America Bulletin, v. 121, p. 599–614, https://doi.org/10.1130/B26352.1.

Lienkaemper, J.J., Pezzopane, S.K., Clark, M.M., and Rymer, M.J., 1987, Fault fractures formed in association with the 1986 Chalfant Valley, California, earthquake sequence: Preliminary report: Bulletin of the Seismological Society of America, v. 77, p. 297–305.

Lifton, Z.M., 2012, Owens Valley, California, 2012 airborne LiDAR: National Center for Airborne Laser Mapping (NCALM), distributed by OpenTopography, https://doi.org/10.5069/G9FF3Q99 (accessed 23 May 2013).

Lifton, Z.M., Newman, A.V., Frankel, K.L., Johnson, C.W., and Dixon, T.H., 2013, Insights on distributed plate rates across the Walker Lane from GPS geodesy: Geophysical Research Letters, v. 40, p. 4620–4624, https://doi.org/10.1002/grl.50804.

Lifton, Z.M., Newman, A.V., and Frankel, K.L., 2015, Latest Pleistocene and Holocene slip rates on the Lone Mountain fault: Evidence for acceleration slip in the Silver Peak–Lone Mountain extensional complex: Tectonics, v. 34, p. 449–463, https://doi.org/10.1002/2013TC003512.

Lueddecke, S.B., Pinter, N., and Gans, P., 1998, Plio-Pleistocene ash falls, sedimentation, and range-front faulting along the White-Inyo Mountains front, California: Journal of Geology, v. 106, p. 511–522, https://doi.org/10.1086/516038.

Machette, M.N., Slate, J.L., and Phillips, F.M., 2008, Terrestrial Cosmogenic-Nuclide Dating of Alluvial Fans in Death Valley, California: U.S. Geological Survey

Professional Paper 1755, 45 p., https://doi.org/10.3133/pp1755.

McCaffrey, R., 2005, Block kinematics of the Pacific–North America plate boundary in the southwestern United States from inversion of GPS, seismological, and geologic data: Journal of Geophysical Research, v. 110, B07401, https://doi.org/10.1029/2004JB003307.

McKee, E.H., Diggles, M.F., Donahoe, J.L., and Elliot, G.S., 1982, Geologic Map of the White Mountains Wilderness and Roadless Areas, California, and Nevada: U.S. Geological Survey Miscellaneous Field Studies Map MF-1361-A, scale 1:62,500.

Mériaux, A.-S., Van der Woerd, J., Tapponnier, P., Ryerson, F.J., Finkel, R.C., Lasserre, C., and Xu, X., 2012, The Pingding segment of the Altyn Tagh fault (91°E): Holocene slip-rate determination from cosmogenic radionuclide dating of offset fluvial terraces: Journal of Geophysical Research, v. 117, B09406, https://doi.org/10.1029/2012JB009289.

Milliner, C.W., Dolan, J.F., Hollingsworth, J., Leprince, S., Ayoub, F., and Sammis, C.G., 2015, Quantifying near-field and off-fault deformation patterns of the 1992 Mw 7.3 Landers earthquake: Geochemistry Geophysics Geosystems, v. 16, no. 5, p. 1577–1598, https://doi.org/10.1002/2014GC005693.

Nagorsen-Rinke, S., Lee, J., and Calvert, A., 2013, Pliocene sinistral slip across the Adobe Hills, eastern California–western Nevada: Kinematics of fault slip transfer across the Mina deflection: Geosphere, v. 9, p. 37–53, https://doi.org/10.1130/GES00825.1.

Nishiizumi, K., Imamura, M., Caffee, M.W., Southon, J.R., Finkel, R.C., and McAninch, J., 2007, Absolute calibration of [10]Be AMS standards: Nuclear Instruments & Methods in Physics Research, Section B, Beam Interactions with Materials and Atoms, v. 258, p. 403–413, https://doi.org/10.1016/j.nimb.2007.01.297.

Oldow, J.S., Kohler, G., and Donelick, R.A., 1994, Late Cenozoic extensional transfer in the Walker Lane strike-slip belt, Nevada: Geology, v. 22, p. 637–640, https://doi.org/10.1130/0091-7613(1994)022<0637:LCETIT>2.3.CO;2.

Oskin, M., Perg, L., Shelef, E., Strane, M., Gurney, E., Singer, B., and Zhang, X., 2008, Elevated shear zone loading rate during an earthquake cluster in eastern California: Geology, v. 36, p. 507–510, https://doi.org/10.1130/G24814A.1.

Pérouse, E., and Wernicke, B.P., 2017, Spatiotemporal evolution of fault slip rates in deforming continents: The case of the Great Basin region, northern Basin and Range Province: Geosphere, v. 13, no. 1, p. 112–135, https://doi.org/10.1130/GES01295.1.

Reheis, M.C., and Dixon, T.H., 1996, Kinematics of the Eastern California shear zone: Evidence for slip transfer from Owens and Saline Valley fault zones to Fish Lake Valley fault zone: Geology, v. 24, p. 339–342, https://doi.org/10.1130/0091-7613(1996)024<0339:KOTECS>2.3.CO;2.

Reheis, M.C., and Sawyer, T.L., 1997, Late Cenozoic history and slip rates of the Fish Lake Valley, Emigrant Peak, and Deep Springs fault zones, Nevada and California: Geological Society of America Bulletin, v. 109, p. 280–299, https://doi.org/10.1130/0016-7606(1997)109<0280:LCHASR>2.3.CO;2.

Reheis, M.C., Sawyer, T.L., Slate, J.L., and Gillispie, A.R., 1993, Geologic Map of Late Cenozoic Deposits and Faults in the Southern Part of the Davis Mountain 15′ Quadrangle, Esmeralda County, Nevada: U.S. Geological Survey Miscellaneous Investigations Map I-2342, scale 1:24,000.

Reitman, N.G., Mueller, K.J., Tucker, G.E., Gold, R.D., Briggs, R.W., and Barnhart, K.R., 2019, Offset channels may not accurately record strike-slip fault displacement: Evidence from landscape evolution models: Journal of Geophysical Research–Solid Earth, v. 124, p. 13427–13451, https://doi.org/10.1029/2019JB018596.

Schwartz, D.P., and Coppersmith, K.J., 1984, Fault behavior and characteristic earthquakes: Examples from the Wasatch and San Andreas fault zones: Journal of Geophysical Research–Solid Earth (1978–2012), v. 89, p. 5681–5698.

Sheehan, T.P., 2007, Evolution of Neogene Fault Populations in Northern Owens Valley, California,

and Implications for the Eastern California Shear Zone [Ph.D. thesis]: New Orleans, Louisiana, Tulane University, 203 p.

Smith, K.D., and Priestley, K.F., 2000, Faulting in the 1986 Chalfant, California, sequence: Local tectonics and earthquake source parameters: Bulletin of the Seismological Society of America, v. 90, p. 813–831, https://doi.org/10.1785/0119990129.

Stockli, D.F., Dumitru, T.A., McWilliams, M.O., and Farley, K.A., 2003, Cenozoic tectonic evolution of the White Mountains, California and Nevada: Geological Society of America Bulletin, v. 115, p. 788–816, https://doi.org/10.1130/0016-7606(2003)115<0788:CTEOTW>2.0.CO;2.

Stone, J.O., 2000, Air pressure and cosmogenic isotope production: Journal of Geophysical Research, v. 105, p. 23753–23759, https://doi.org/10.1029/2000JB900181.

Thatcher, W., 2009, How the continents deform: The evidence from tectonic geodesy: Annual Review of Earth and Planetary Sciences, v. 37, p. 237–262, https://doi.org/10.1146/annurev.earth.031208.100035.

Wallace, R.E., 1987, Grouping and migration of surface faulting and variations in slip rates on faults in the Great Basin Province: Bulletin of the Seismological Society of America, v. 77, p. 868–876.

Wesnousky, S.G., 2005, The San Andreas and Walker Lane fault systems, western North America: Transpression, transtension, cumulative slip and the structural evolution of a major transform plate boundary: Journal of Structural Geology, v. 27, p. 1505–1512, https://doi.org/10.1016/j.jsg.2005.01.015.

Zechar, J.D., and Frankel, K.L., 2009, Incorporating and reporting uncertainties in fault slip rates: Journal of Geophysical Research, v. 114, B12407, https://doi.org/10.1029/2009JB006325.

Zehfuss, P.H., Bierman, P.R., Gillespie, A.R., Burke, R.M., and Caffee, M.W., 2001, Slip rates on the Fish Springs fault, Owens Valley, California, deduced from cosmogenic ^{10}Be and ^{26}Al and soil development on fan surfaces: Geological Society of America Bulletin, v. 113, p. 241–255, https://doi.org/10.1130/0016-7606(2001)113<0241:SROTFS>2.0.CO;2.

Zielke, O., and Arrowsmith, J.R., 2012, LaDiCaoz and LiDARimager—MATLAB GUIs for LiDAR data handling and lateral displacement measurement: Geosphere, v. 8, p. 206–221, https://doi.org/10.1130/GES00686.1.

Zinke, R., Hollingsworth, J., and Dolan, J.F., 2014, Surface slip and off-fault deformation patterns in the 2013 MW 7.7 Balochistan, Pakistan, earthquake: Implications for controls on the distribution of near-surface coseismic slip: Geochemistry Geophysics Geosystems, v. 15, no. 12, p. 5034–5050, https://doi.org/10.1002/2014GC005538.